DEVELOPING SILICON-BASED THERMOELECTRICS FOR COOLING APPLICATIONS

A Dissertation
Presented to
The Academic Faculty

by

David Misha Rodin

In Partial Fulfillment
of the Requirements for the Degree
of Doctor of Philosophy in the
George W. Woodruff School of Mechanical Engineering

Georgia Institute of Technology
May 2019

DEVELOPING SILICON-BASED THERMOELECTRICS FOR COOLING APPLICATIONS

Approved by:

Dr. Shannon Yee, Advisor
School of Mechanical Engineering
Georgia Institute of Technology

Dr. Satish Kumar
School of Mechanical Engineering
Georgia Institute of Technology

Dr. Samuel Graham
School of Mechanical Engineering
Georgia Institute of Technology

Dr. Martin Maldovan
School of Chemical and Biomolecular Engineering
Georgia Institute of Technology

Dr. Zhuomin Zhang
School of Mechanical Engineering
Georgia Institute of Technology

Date Approved: December 14, 2018

To my family, advisor, and committee.

ACKNOWLEDGEMENTS

First and foremost, I would like to acknowledge my research advisor, Dr. Shannon Yee, for accepting me into his first cohort of students, for his tireless support through the ups and downs of graduate school, for convincing me to rededicate myself to earning a doctorate, and for his dedication to my own development, even when it was not directly beneficial to our group's research goals. Shannon was extremely supportive of my work with the Energy Club @ Georgia Tech, which ended up being one of the most memorable experiences during my time at Georgia Tech. I consider myself extremely fortunate to have worked with Shannon.

I would also like to acknowledge John Carberry, Robert Tesch, and Devin Roberts of the Silniva Corporation. I'm not sure I would have finished my Ph.D. without the opportunity to work with Silniva, and I am incredibly grateful for the time we spent working together.

Finally, I would like to thank my thesis committee for providing valuable feedback on my work. Peer review is the foundation of science, and the discussions with my committee were invaluable for my work and my own development. Specifically, I would like to thank Dr. Satish Kumar and Dr. Martin Maldovan for their tough questions and insights on how to build on my work. I would like to thank Dr. Samuel Graham for his experimental suggestions and supporting me on his Interface MURI during my last semester. Finally, I would like to thank Dr. Zhuomin Zhang for stumping me during my proposal presentation and motivating me to go back and learn solid-state physics.

TABLE OF CONTENTS

LIST OF TABLES

LIST OF FIGURES

LIST OF SYMBOLS AND ABBREVIATIONS

a Particle radius

A_1 Impurity scattering fitting parameter

A_2 Umklapp scattering fitting parameter

A_3 Boundary scattering fitting parameter

A_c Pellet cross-sectional area

A_P Total heating power of pump beam

C Volumetric specific heat

C_g Constant for pressure-dependent thermal conductivity of an ideal gas

C_{ph} Phonon specific heat

C_u Umklapp scattering exponential fitting parameter

D Thermal diffusivity

d_b Distance between boundaries containing ideal gas

e Electron charge

E Energy level

E_c Conduction band edge energy level

E_f Fermi level

E_g Band gap energy

E_v Valence band edge energy level

f Heating frequency

f_0 Equilibrium Fermi-Dirac distribution

g Density of states

G Thermal interface conductance

G_q Hankel transform of frequency-domain solution for periodic point source

$\hbar$ Planck constant

J_0 Bessel function of the first kind, zeroth-order

K Neck curvature

k_b Boltzmann constant

L Characteristic scattering length scale

L_{air} Distance between adjacent pore boundaries

L_c Length scale of thermal gradient

L_p Thermal penetration depth

n Dopant concentration

n_i Intrinsic carrier concentration

P Hankel transform of pump's heating profile

P_o Pre-exponential factor for temperature-dependent vapor pressure

p_s Spatial intensity profile of the offset probe beam

P_s Hankel transform of offset probe beam's intensity profile

P_v Vapor pressure

q Phonon wavevector

q'' Heat flux

Q_{vap} Heat of vaporization

R Electrical resistance

r Sensor radius

Ra Rayleigh number

r_κ Characteristic neck size based on thermal conductivity measurements

r_σ Characteristic neck size based on electrical conductivity measurements

s Dummy integration variable

S	Seebeck coefficient
S_B	Bulk Seebeck coefficient
S_{eff}	Effective Seebeck coefficient
S_β	Sensitivity parameter
T	Temperature
t	Pellet thickness
T_C	Cold-side temperature
t_{char}	Characteristic measurement time
T_H	Hot-side temperature
t_m	Measurement time
U	Measurement uncertainty
v	Group velocity
w	Beam spot $1/e^2$ radius
x	Neck size during sintering
zT	Material figure-of-merit
α	Attenuation constant for Akhieser damping
γ	Grüneisen parameter
γ_s	Surface free energy
Δ_p	Probing depth
ΔT	Junction temperature difference
ε	Porosity
η	Anisotropy ratio
θ	Phase lag
κ	Thermal conductivity
$\kappa_{/\!/}$	In-plane thermal conductivity

$\kappa_{\perp}$	Through-plane thermal conductivity
κ_{eff}	Effective thermal conductivity
$\kappa_{eff,domain}$	Effective thermal conductivity of domain
$\kappa_{eff,random}$	Effective thermal conductivity of packed bed in close-random arrangement
κ_{exp}	Experimentally-measured thermal conductivity
κ_{L}	Contribution from longitudinal phonons
κ_{TO}	Contribution from low-frequency transverse phonons
κ_{TU}	Contribution from high-frequency transverse phonons
Λ	Phonon mean-free-path
λ	Laser wavelength
ρ	Density
σ	Electrical conductivity
σ_{B}	Bulk electrical conductivity
σ_{eff}	Effective electrical conductivity
τ	Scattering time
τ_{A}	Scattering time from Akhieser damping
τ_{c}	Combined scattering time
τ_{N}	Scattering time contribution from normal processes
ω	Angular frequency
Ω	Atomic volume
$\omega_{0,\lambda}$	Maximum phonon frequency for mode λ
APT	Atom probe tomography
BB-FDTR	Broadband frequency-domain thermoreflectance
BP	Bandpass filter
BS	Beam splitter

BTE	Boltzmann transport equation
CB	Conduction band
COP	Coefficient of performance
c-Si	Crystalline silicon
DOS	Density of states
EOM	Electro-optic modulator
FDTR	Frequency-domain thermoreflectance
GWP	Global warming potential
HFC	Hydrofluorocarbon
HOPG	Highly-oriented pyrolytic graphite
HWP	Half-wave plate
ISO	Optical isolator
LD	Laser diffraction
MFP	Mean free path
np-Si	Nano-porous silicon
OBJ	Objective
PBS	Polarizing beam splitter
PD	Photodiode
PSD	Particle size distribution
PWE	Plane-wave expansion
QWP	Quarter-wave plate
RTA	Relaxation-time approximation
SEM	Scanning electron microscope
TDTR	Time-domain thermoreflectance
TE	Thermoelectric

TEC	Thermoelectric cooler
TPS	Transient plane source
TTR	Transient thermoreflectance
VCT	Vapor-compression technologies

SUMMARY

Research on silicon thermoelectric coolers lies at the intersection of semiconductor physics, nanoscale heat transfer, industrial manufacturing, and device engineering. The electronic properties of doped silicon ($\sigma \approx 50{,}000$ S/m and $S \approx 200$ μV/K at 10^{20} cm^{-3}) are highly desirable, but the intrinsic thermal conductivity is at least two orders of magnitude too high for thermoelectric applications. The phononic contributions to the thermal conductivity dominate in silicon and have mean free paths that span a wide range of length scales at room temperature. Conversely, electronic contributions to the thermal conductivity span a much narrower mean free path spectrum at smaller length scales. The thermoelectric potential of bulk silicon may be realized in nanoporous silicon (np-Si) that selectively impedes phonons. The task of minimizing thermal conduction, without significantly affecting the electronic transport, represents an opportunity to use recent scientific understanding of thermal transport in silicon for the important engineering application of cooling. Furthermore, the development of np-Si creates an opportunity for experimental measurements that may further the scientific understanding of nanoscale physics. This dissertation includes (i) a scalable fabrication process used to produce np-Si from degenerately-doped silicon powders, (ii) experimental measurements of the thermoelectric properties of the np-Si samples, (iii) microstructural and compositional characterization of the np-Si samples, (iv) a numerical model that applies the characterization results to predict the effective thermoelectric properties of np-Si, and (v) an augmentation of frequency-domain thermoreflectance to measure the thermal conductivity of anisotropic samples.

CHAPTER 1. INTRODUCTION TO THERMOELECTRICS

The vast majority of heating, ventilation, air conditioning, cooling, and refrigeration devices are based on vapor-compression technologies (VCT) that use refrigerants with high global warming potential.[1] Hydrofluorocarbons (HFCs) are the most prominent refrigerants in use today and global demand is growing at 10 to 15% per year. Under current growth models, the contribution of HFCs to global warming has been estimated at 0.5°C by the end of the century.[2] However, this trend could be mitigated due to the relatively short atmospheric lifetime of most HFCs (~15 years).[3] The replacement of VCT with a more environmentally-friendly technology has clear benefits, but rapid and widespread adoption may only be possible if the new technology is economically competitive with VCT. Therefore, any alternative to VCT must be capable of pumping heat with a coefficient of performance (COP) that is comparable to VCT, as this directly translates to the operating cost of the device.

Thermoelectric coolers (TECs) pump heat via the Peltier effect, as shown in Figure 1. TECs provide cooling with no global warming potential, operate reliably without moving parts, and can provide a high capacity for both heating and cooling in a scalable device.[4, 5] However, current TEC technology is not competitive with VCT on the basis of COP and the market penetration has been limited to niche applications. The COP of a TEC is a function of geometry, operating conditions, heat exchanger performance, and thermoelectric properties. The relevant materials properties can be lumped into a dimensionless material figure of merit $zT = S^2\sigma T / \kappa$ to provide a formulation for the maximum achievable COP for cooling

$$COP_{\max} = \frac{T_C}{\Delta T}\left(\frac{(1+zT)^{1/2} - T_H / T_C}{(1+zT)^{1/2}+1}\right), \quad (1)$$

where S is the Seebeck coefficient (μV/K), σ is the electrical conductivity (S/m), κ is the thermal conductivity (W/m-K), and T_H and T_C are the hot and cold side temperatures (K), respectively. Bulk crystalline semiconductors, notably Bi_2Te_3, can be optimized via doping to $zT \approx 1$, but further improvements can be achieved through the decoupling of S, κ, and σ via nanostructuring.[6, 7]

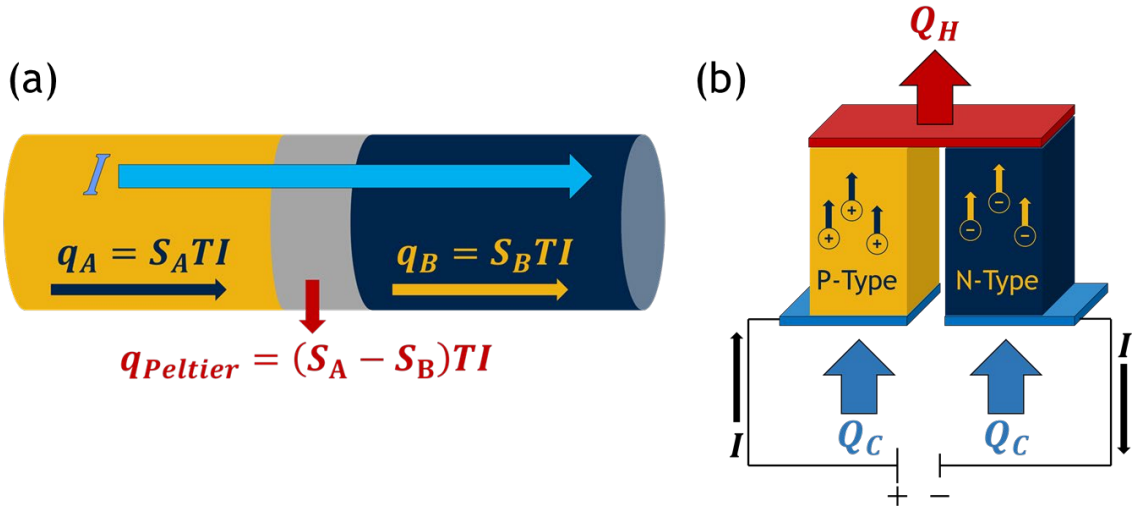

Figure 1 - (a) Diagram of electrical current passing through a junction of dissimilar materials, resulting in the release of Peltier heat. (b) A TEC using traditional flat-plate geometry. Alternating p-type and n-type legs are arranged electrically in series and thermally in parallel, resulting in a net heat pumping effect when electrical current is applied.

1.1 Silicon Thermoelectrics

1.1.1 Silicon's Potential for Thermoelectric Applications

The potential of silicon (c-Si) as a thermoelectric material derives from its natural abundance, low cost, attractive thermoelectric properties (*e.g.*, power factor, $S^2\sigma$), and mature manufacturing processes.[8] However, the high thermal conductivity of bulk intrinsic (*i.e.* undoped) silicon ($\kappa \approx 149$ W/m-K) results in a low zT. A comparison between bulk degenerate (~$7x10^{19}$ atoms/cm^3) silicon[9] and nanostructured p-type $Bi_{0.48}Sb_{1.52}Te_3$[10] is shown in Table 1. The thermal conductivity of silicon must be reduced by at least two orders of magnitude before it can become an economically competitive TE material.

Table 1 - Comparison of approximate bulk thermoelectric properties between state-of-the-art bismuth animoney telluride and bulk degenerate silicon at room temperature.

Property	**$Bi_{0.48}Sb_{1.52}Te_3$** (p-type, n=$3x10^{19}$ cm^{-3})	**Degenerate Silicon** (p-type, n=$7x10^{19}$ cm^{-3})
Electrical Conductivity (σ)	~125 kS/m	~45 kS/m
Seebeck Coefficient (S)	~205 μV/K	~205 μV/K
Thermal Conductivity (κ)	~1.15 W/m-K	~87[(a)] W/m-K
Power Factor ($S^2\sigma$)	~5,250 μW/m-K^2	~1,900 μW/m-K^2
Figure-of-Merit (zT)	~1.5	~0.007

[(a)] Thermal conductivity of degenerate silicon (~87 W/m-K) is reduced below intrinsic silicon (~149 W/m-K) due to impurity scattering.

The study of nanostructured silicon for thermoelectric applications has been a subject of recent interest.[11-15] The tunable size effects in silicon nanostructures[13, 16]

can be used to exploit that electron transport in silicon occurs at nanoscale dimensions[17] whereas phononic size effects are observed in structures as large as 1 μm.[18, 19] Thus, a well fabricated structure may be able to sufficiently reduce silicon's thermal conductivity while leaving the desirable electrical properties intact. [11, 15, 20, 21]

1.1.2 Nanostructured Silicon Thermoelectrics

The use of lower dimensional structures for the selective reduction of thermal conductivity was introduced over 25 years ago by Hicks and Dresselhaus, and subsequent advancements in the understanding of nanoscale transport properties has led to significant improvements in the thermoelectric properties of silicon.[22, 23] The most notable achievements include experimental measurements of silicon nanowires[24] ($zT \approx 0.6$) and porous silicon membranes[11] ($zT \approx 0.4$) at room temperature. Although these reports demonstrate the ability to enhance zT via nanostructuring, the commercialization of these materials is challenging because the reduced dimensionality of these materials makes it difficult to integrate them into existing device architectures.[23]Progress towards novel device architectures is one approach towards the commercialization of nanostructured thermoelectric materials.[25, 26] However, a more straightforward approach involves the fabrication of nanostructured materials that can be readily integrated into existing devices.[27, 28]

Bulk nanostructured porous silicon (np-Si) is an alternative geometry that incorporates silicon nanoparticles into a porous heterostructure with outer dimensions on the scale of millimetres. Computational studies of superlattice structures have shown that the desirable reduction in the thermal conductivity of nanostructured materials does not

require exact geometries or perfect interfaces[29], but is primarily driven by the high density of interfaces.[30] Bulk nanostructures retain the high density of interfaces without the need for controlled geometries, and can therefore be manufactured using industrial techniques and integrated into existing devices. [8, 15, 20], [27, 31] Bux et al. fabricated n-type np-Si using ball milling and hot pressing to achieve $zT \approx 0.7$ at 1200 K ($zT \approx 0.04$ at 300 K).[27] Kessler et al. synthesized nanoparticles from a scalable gas phase process with production rates approaching ~1 kg/h, and used a current-assisted sintering technique to achieve $zT \approx 0.45$ at 1000 K ($zT \approx 0.1$ at 300 K).[31] However, the fabrication of np-Si with competitive TE properties at room temperature remains an unsolved challenge.

1.2 Experimental Measurement of Nanoscale Thermal Transport

The principle of thermoelectric improvements via nanostructuring has been robustly demonstrated, but the optimization of these structures is contingent upon further developments in the understanding of nanoscale thermal transport.[14] Significant progress has been achieved through atomistic simulations and analytical models, but experimental validation of these results is an ongoing challenge.[14, 32-35]

In recent years, a set of experimental techniques that rely on transient thermoreflectance (TTR) have shown potential to measure the accumulation of thermal conductivity as a function of phonon mean-free-path, Λ.[36] TTR techniques, most notably time-domain thermoreflectance (TDTR) and frequency-domain thermoreflectance (FDTR), apply a periodic heat source to a sample and observe the temperature-dependent variation in the sample's reflectance.[37-40] The relationship between the heat source and surface reflectance is used to extract information about the thermal properties of the

sample, most often the thermal conductivity of bulk materials, thin films, and the thermal interface conductance between materials. These techniques are advantageous for studying nanoscale phonon transport because of their ability to control the length scale of the temperature gradient, L_c, by controlling either the heating laser's spot size, w_0, or the thermal penetration depth, L_p, which can be indirectly controlled due to the.[36] Both TDTR and FDTR have observed a reduction in the experimentally-observed thermal conductivity κ_{exp} when L_c is commensurate with the mean-free-path of phonons.[41-44] The initial interpretation of κ_{exp} vs. L_c involved the application of a step-wise suppression function where only phonons with $\Lambda < L_c$ contributed to κ_{exp}.[43] Mathematically, this description takes the form

$$\kappa_{\exp}(L_c) = \int_0^{L_p} \kappa(\Lambda) d\Lambda \,, \tag{2}$$

where Λ is the phonon MFP and $\kappa(\Lambda)$ is the thermal conductivity accumulation function. Koh and Cahill were the first to use Equation 2 to measure $\kappa(\Lambda)$ in bulk semiconductor alloys by performing TDTR measurement at multiple heating frequencies.[42] Regner et al.[19, 45] and Freedman et al.[44] applied the same approach using FDTR and observed a similar relationship between κ_{exp} and L_p. Minnich et al. performed TDTR measurements using beam spot diameters of 15 μm, 30 μm, and 60 μm at temperatures ranging from 90 K to 300 K. The measured thermal conductivity was independent of beam diameter at T = 300 K, but at T = 90 K the 60 μm beam measured a thermal conductivity of 630 W/m-K whereas the 15 μm beam returned a measured value of 480 W/m-K. Both of these measured values were below the literature value of 1000 W/m-K.[46] Minnich et al. hypothesized that the heated region was at local equilibrium when the heater dimensions (i.e. beam

diameter) was larger than the phonon MFP, but ballistic transport affected the measurement when $2w_0 < \Lambda$. This hypothesis was strengthened by agreement between the measured values and the expected values obtained by setting $L_c = 2w_0$ in Equation 2.[41] The resulting thermal conductivity accumulation functions, all measured on silicon at room temperature, are shown in Figure 2. Wilson and Cahill used TDTR with offset beams to measure κ as a function of beam diameter, heating frequencies, temperature, and impurity concentrations, but were unable to explain their results using the traditional diffusive model. Their analysis called for a more nuanced model of ballistic transport in TTR measurements, which will be discussed in the following section.[47]

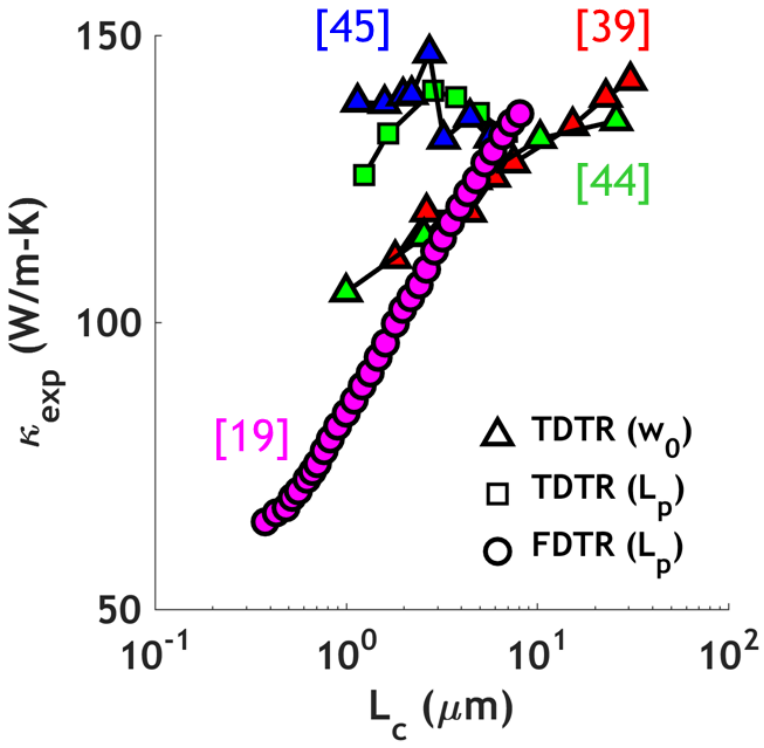

Figure 2 - Experimental measurements of the thermal conductivity accumulation function of silicon at room temperature. Measurements using TDTR include the use of both spot size (w_0) and penetration depth (L_p) as the limiting conduction length scale (L_c). Measurements using FDTR only rely on controlling L_p.

The MFP accumulation functions shown in Figure 2 are generated by fitting TDTR and FDTR data to a diffusive model (i.e. based on Fourier theory), and the measured thermal conductivity value is based on agreement between the model and the experimental data. However, this approach assumes that thermal transport in the quasiballistic regime (i.e. the transitional regime between diffusive and ballistic transport) can be described by applying a reduced thermal conductivity to the traditional diffusive model. Wilson and Cahill investigated this assumption by performing a set of TDTR measurements to determine when and how Fourier theory will lose its ability to solve nanoscale heat transfer problems.[47] Measurements were performed on room-temperature silicon using offset pump and probe beams to allow for independent measurements of through-plane thermal conductivity, $\kappa_{\perp}$, and in-plane thermal conductivity, $\kappa_{\parallel}$.[48] Wilson and Cahill were able to reproduce the bulk literature value of 140 W/m-K for all beam offset distances using the 10 μm beam. When the beam diameter was reduced to 1 μm and the beams were co-aligned, they measured a reduced value of κ_{exp} = 105 W/m-K which was consistent with the findings of Minnich et al.[46] However, their measured value of 105 W/m-K failed to predict the experimental data for the case of offset beams. When independent values for $\kappa_{\perp}$ and $\kappa_{\parallel}$ were considered, the measured values of $\kappa_{\perp}$ = 140 W/m-K and $\kappa_{\parallel}$ = 80 W/m-K provided excellent agreement with experimental data across all beam-offset distances. Wilson and Cahill concluded that reducing the beam diameter leads to a reduction in $\kappa_{\parallel}$ with a negligible effect on $\kappa_{\perp}$. More broadly, they concluded that a reduction in $\kappa_{\parallel}$ would occur when $w_0 < \Lambda$ and a reduction in $\kappa_{\perp}$ would occur when $L_p < \Lambda$ and in-plane conduction was negligible (i.e. $L_p << w_0$).

Wilson and Cahill demonstrated the importance of using an anisotropic model to observe and interpret reductions in the thermal conductivity measured by TDTR and FDTR experiments.[47] Other interpretations have incorporated more nuanced suppression functions derived from solutions to the Boltzmann transport equation (BTE) under the relaxation-time approximation.[49-52] Vermeersch et al. suggested that super-diffusive Lévy dynamics could be used to explain the reduction in κ_{exp} at small timescales and length scales.[53, 54] Currently, the interpretation of these measurements remains an open question and both experimental and theoretical are viable approaches.

1.3 Scope of Present Work

The aim of the present work is to advance the understanding of nanoscale thermal transport properties in np-Si. This will be accomplished through the investigation of three critical questions:

To what degree can the thermal conductivity of np-Si be reduced to create a high-performance thermoelectric material?

The selective reduction of silicon's thermal conductivity via nanostructuring has been robustly demonstrated.[11, 15, 20, 21] However, a reduction of at least two orders of magnitude is necessary for np-Si to be realized as a high-performance thermoelectric material. This work reports measurements of both the electrical and pressure-dependent thermal properties of np-Si samples. The experimental measurements demonstrate a strong selective reduction in the thermal conductivity of np-Si, but the improvements in the TE properties were not sufficient ($ZT < 0.4$ at room temperature) to demonstrate steady cooling.

To what degree is the reduction in thermal conductivity observed in np-Si consistent with current understanding of phonon transport in c-Si?

This work presents an analysis on the applicability of relaxation-time phonon transport models to predict the effective thermal conductivity of np-Si. As a starting point, the Holland thermal conductivity model is used to generate a set of phonon MFP accumulation functions that incorporate boundary scattering, impurity scattering, phononic crystal effects, and, for the first time, Akhieser damping and dopant concentration. The MFP accumulation functions are applied to a simplified np-Si geometry and a finite-element analysis (FEA) is used to predict the effective thermal conductivity of np-Si. The applicability of each accumulation function to np-Si is evaluated based on agreement between model predictions and experimental measurements of effective thermal conductivity. SEM images, electrical conductivity measurements, and the relationship between air pressure and effective conductivity is used to validate the use of a simplified geometry in the FEA.

To what degree can frequency-domain thermoreflectance (FDTR) be used to make observations about thermal transport in np-Si?

The use of FDTR has attracted considerable attention for its potential to directly measure phonon mean free path (MFP) accumulation in crystalline silicon (c-Si).[43, 45] However, the reproducibility of this work has not been studied. Furthermore, Wilson et al. have suggested that a failure to account for anisotropic thermal conductivities can contribute to erroneous interpretations of high frequency data.[47] The present work includes attempts to reproduce the FDTR measurements on silicon, and presents an

augmentation to traditional FDTR that enables simultaneous measurement of in-plane and through-plane thermal conductivity for anisotropic samples to evaluate the claims of anisotropic thermal conductivities.

CHAPTER 2. THERMOELECTRIC TRANSPORT IN SILICON

2.1 Charge Transport in Crystalline Silicon

The transport of charge carriers in c-Si is described by the band transport model derived from the Boltzmann transport equation (BTE).[35] In this model, the bulk electrical conductivity is formulated as:

$$\sigma_B = -\frac{e^2}{3}\int \tau v^2 g \frac{\partial f}{\partial E} dE = -\frac{e^2}{3}\int \sigma(E) dE \,, \tag{3}$$

where E is the electron energy, ν is the carrier velocity, e is the elementary charge, τ is the scattering time, g is the electronic density of states, $\sigma(E)$ is the differential electrical conductivity, and f is the equilibrium Fermi-Dirac distribution:

$$f = \frac{1}{e^{(E-E_f)/k_bT}+1}, \tag{4}$$

$$\frac{\partial f}{\partial E} = f'(E) = -\frac{e^{(E-E_f)/k_bT}}{k_bT(e^{(E-E_f)/k_bT}+1)^2}. \tag{5}$$

where E_f is the Fermi level and k_b is the Boltzmann constant. The density of states scales as $g \propto E^{1/2}$ in the conduction/valence bands and, by definition, $g = 0$ in the band gap. The Fermi derivative $f'(E)$ peaks at $E = E_f$ and decays with an exponential decay length on the order of $k_bT << E_g$.

The differential electrical conductivity is also found in the formulation for the Seebeck coefficient

$$S_B = -\frac{1}{eT}\frac{\int_0^\infty \sigma(E)(E - E_f)dE}{\sigma_B}. \tag{6}$$

Mathematically, the Seebeck coefficient is related to the asymmetry in the differential electrical conductivity about the Fermi level. The Seebeck coefficient can be physically understood by examining the diffusion behavior of electrons in the presence of a temperature gradient. From Equation 4, an increase in temperature causes the promotion of electrons from the valence band to the conduction band, which results in an increased concentration of "hot" electrons ($E > E_f$) and a decrease in the concentration of "cold" electrons ($E < E_f$). Therefore, the temperature gradient creates a parallel concentration gradient of hot electrons and an antiparallel concentration gradient of cold electrons. The concentration gradients drive the diffusion of mobile charge carriers (electrons for n-type materials and holes for p-type materials) towards the cold side, resulting in the accumulation of an internal electric field that resists the charge diffusion. Equilibrium is reached when the diffusive current is nullified by the opposing drift current from the electric field, and the Seebeck voltage is the steady-state voltage accumulated under open-circuit conditions. If the hot and cold electrons are equally conductive (*i.e.,* the material is ambipolar and $\sigma(E)$ is symmetric about E_f), the diffusive currents counteract each other and the temperature gradient does not generate a Seebeck voltage.

2.1.1 Effect of Dopant Atoms on Electrical Properties

The introduction of impurity dopant atoms can shift the Fermi level, thereby affecting the electrical properties of silicon. The relationship between doping concentration and electrical conductivity can be understood by examining the $g(E)f'(E)$ product in Equation 2. The mass action law and charge neutrality law can be applied to derive a relationship between the Fermi level and carrier concentration

$$E_f(n) = \frac{E_c + E_v}{2} \pm k_b T ln\left(\frac{n}{n_i}\right), \tag{7}$$

where E_c and E_v are the energy levels for the conduction band edge and valence band edge, respectively, n_i is the intrinsic carrier concentration, and n is the extrinsic carrier concentration. The second term of Equation 7 is positive when electrons are the majority carrier (n-type) and negative when holes are the majority carrier (p-type). For intrinsic silicon, $n = n_i$ and E_f falls in the center of the band gap. When dopant impurities are introduced, n is increased beyond n_i and the Fermi level will shift towards the conduction band (n-type) or valence band (p-type), resulting in an increase in the density of free carriers and electrical conductivity. The relationship between E_f, $g(E)$, and $f'(E)$ is visualized for various doping levels in Figure 3.

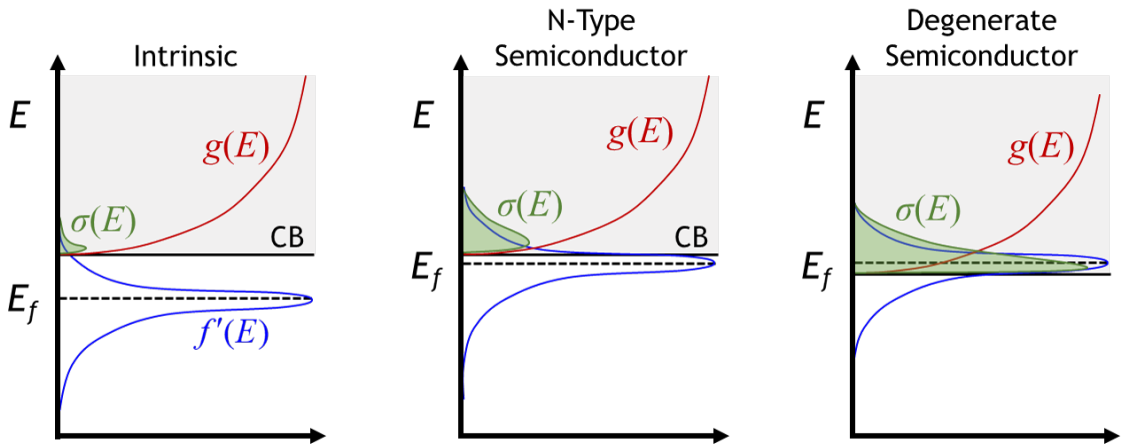

Figure 3 - Relationship between E_f, g(E), f′(E) , and σ(E) for various doping concentrations. The Fermi level for intrinsic silicon is far from the conduction band edge (CB) and the density of states, g(E), shows very little overlap with f′(E). As the doping concentration is increased, the Fermi level approaches the conduction band edge and the conduction band becomes increasingly populated with electrons, resulting in an increased in $\sigma(E)$. In the case of degenerate semiconductors, the high concentration of dopants causes a shift in the band edge and the Fermi level falls inside the conduction band, resulting in metallic conduction properties (i.e. high electrical conductivity).

The competing trends between the diffusion current and drift current create a natural trade-off between σ and S in doped semiconductors. When dopant concentrations are increased, the Fermi level shifts from the center of the band gap towards a band edge. This results in a higher population of free electrons and an increase to σ_B. However, the shift in Fermi level makes $\sigma(E)$ more symmetric about E_f, resulting in a lower Seebeck coefficient. This trade-off between electrical conductivity and Seebeck coefficient in semiconductors establishes an optimum thermoelectric doping concentration that can be determined through the maximization of the thermoelectric power factor, $S^2\sigma$. For c-Si at 300 K, the optimum doping concentration is on the order of 10^{20} atoms/cm^3, resulting in an optimum power factor of ~2000 and ~5000 μW/m-K^2 for p-type and n-type,

respectively.[55] These power factors are comparable to the ~5000 μW/m-K^2 values that have been reported for zone-melted p-type $Bi_{0.48}Sb_{1.52}Te_3$ and n-type $Bi_2Te_{2.3}Se_{0.7}$.[10, 56]

2.2 Thermal Transport in Crystalline Silicon

The most prevalent models for phonon transport in c-Si rely on a numerical solution to the Boltzmann transport equation (BTE) using the relaxation time approximation (RTA).[14, 57-59] The well-known Callaway model[60] uses a formulation for thermal conductivity under RTA

$$\kappa = \frac{v^2}{2\pi^2}\int C_{ph}(q)\left(1+\frac{\beta}{\tau_N}\right)\tau_c(q)q^2 dq\,, \tag{8}$$

where κ is the lattice thermal conductivity, v is the phonon group velocity, τ_c is the combined relaxation time from all scattering mechanisms, τ_N is the relaxation time exclusively from normal processes, q is the phonon wavevector, and C_{ph} is the phonon specific heat

$$C_{ph} = \frac{\hbar^2\omega^2}{k_b T^2}\frac{e^{\hbar\omega/k_b T}}{\left(e^{\hbar\omega/k_b T}-1\right)^2}\,. \tag{9}$$

The β term in Equation 8 is given by

$$\beta = \frac{\int_0^{\theta/T} \frac{\tau_c x^4 e^x}{\tau_N \left(e^x - 1\right)^2}}{\int_0^{\theta/T} \frac{1}{\tau_N}\left(1 - \frac{\tau_c}{\tau_N}\right)\frac{e^x}{\left(e^x - 1\right)^2} x^4 dx}, \tag{10}$$

and the combined relaxation time is defined using Mathiessen's rule

$$\tau_c^{-1} = A_1\omega^4 + A_2 T\omega^2 \exp(C_u / T) + A_3 v / L\,, \tag{11}$$

where ω is the phonon frequency, L is the characteristic length scale between boundaries, $A_1\omega^4$ represents the scattering rate contribution from point impurities (e.g. dopant atoms), $A_2T\omega^2\exp(C_u/T)$ represents the scattering rate contribution from phonon-phonon processes, and $A_3 v / L$ represents the scattering rate contribution from boundary scattering.[60] The variables A_1, A_2, and A_3 are free parameters obtained by fitting Equation 8 to the temperature-dependent thermal conductivity of silicon. Although the Callaway model can accurately reproduce the temperature-dependent thermal conductivity for silicon between 1 K and 300K, the data above 300K cannot be reproduced when using a single integral.[61] The best-fit Callaway model across a broad temperature range is shown in Figure 4(a).

Holland et al.[61] augmented the Callaway model by splitting the thermal conductivity into the sum of three modal contributions: low-frequency transverse (TO), high-frequency transverse (TU), and longitudinal (L). The modal form of Equation 8 is

$$\kappa = \frac{1}{6\pi^2}\sum_{\lambda}\int_0^{\omega_{0,\lambda}} \frac{\tau(\omega,\lambda)}{v(\omega,\lambda)} C_{ph}(\omega,\lambda)\omega^2 d\omega \tag{12}$$

where ω is the phonon frequency and $\omega_{0,\lambda}$ is the maximum phonon frequency for the mode λ. For each mode, the phonon spectrum and density-of-states (DOS) distribution for silicon are used to determine $v(\omega,\lambda)$ and the fitting procedure is split into three steps: (1) fit for κ_{TU} at T>1000K, (2) use κ_{TU} contribution and fit for κ_L at room temperature, and (3) use κ_{TU} and κ_L contributions to fit for κ_{TO} at low temperatures. Incorporating mode-dependent processes into Callaway's model allows for higher fidelity across all temperature ranges and, more importantly for this work, improves the resolution of A_3 which is critical for determining how thermal conductivity is affected by changing the value of L.[61] The improvement in temperature-dependent fitting and contributions from individual modes are shown in Figure 4(b).

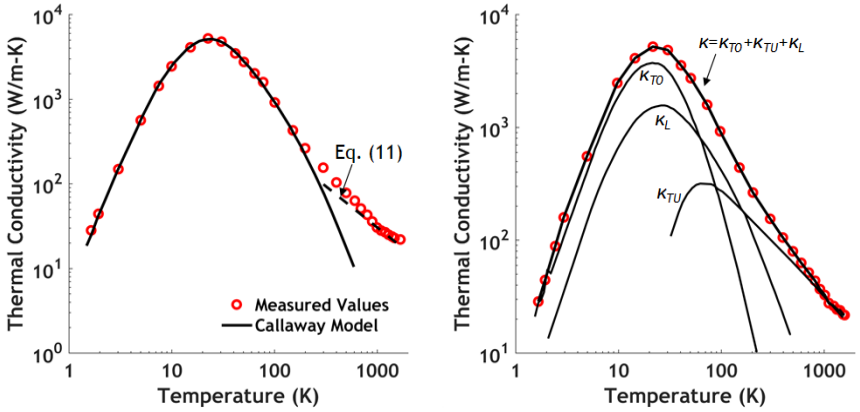

Figure 4 - (a) Comparison between experimentaWl values for temperature-dependent thermal conductivity of silicon and best-fit Callaway model. Holland's mode-dependent approach (Equation 12) is included to show improved fit at high temperature. (b) Comparison between experimental values for temperature-dependent thermal conductivity of silicon and best-fit Holland model. Lattice thermal conductivity is the sum of the contributions from low-frequency transverse modes (κ_{TO}), high-frequency transverse modes (κ_{TU}), and longitudinal modes (κ_L).

The three terms on the right-hand side of Equation 11 represent the impurity scattering rate, Umklapp scattering rate, and boundary scattering rate, respectively. The size-dependence of Equation 12 can be found by varying the value of the limiting conduction length scale (L), and the effect of dopant atoms can be accounted for by establishing a relationship between doping concentration and the fitted value for A_1.

The relationship between doping concentration and A_1 is established by fitting to the temperature-dependent and concentration-dependent thermal conductivity of bulk silicon.[55, 62] The Umklapp scattering rate is assumed to be independent of dopant concentration, so the temperature-dependent thermal conductivity of intrinsic (un-doped) silicon is used to determine the fixed value of A_2 = 4.15e-19 $s^3 \cdot K^{-1}$ and C_u = 140 K. The concentration-dependent thermal conductivity[55] is then used to establish a relationship between doping concentration and A_1. The results of the fitting procedure are shown in Figure 5.

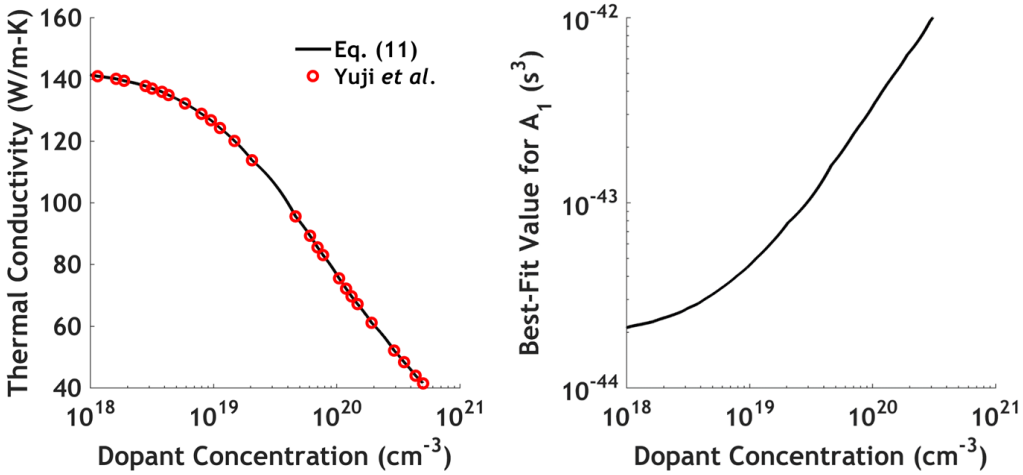

Figure 5 - (a) Setting A_1 as a free fitting parameter allows for strong agreement between Equation 12 and literature values for concentration-dependent thermal conductivity. (b) Relationship between dopant concentration and best-fit value for A_1.

The resulting relationship, which represents an original contribution, enables the use of Equation 12 to predict the size-dependent and concentration-dependent thermal conductivity of c-Si, shown in Figure 6. For conduction length scales less than 100nm, the thermal conductivity predicted by Equation 12 is consistently higher than the predictions from atomistic simulations. This difference is attributed to physical shortcomings of relaxation-time models and the use of approximate expressions for the scattering rates in Equation 11 as compared to atomistic simulations.[32, 63] However, the ability of the Equation 12 to evaluate the thermal conductivity of silicon as a function of doping concentration without significant computational resources make it useful for the present study.

The gaseous pores may also contribute to the heat transfer behavior of np-Si. For microporous solids, the Rayleigh number is low (Ra<<1) and the effects of natural convection may be ignored. In this case, the thermal conductivity of the gas is formulated as

$$\kappa_{air} = \frac{\kappa_0}{1 + C_g T / P d_b}, \tag{13}$$

where κ_0 is the thermal conductivity of air at standard temperature T and pressure P, C is a gas-dependent constant based on empirical correlations from experimental measurements, and d_b is the distance between two adjacent boundaries in the direction of the temperature gradient.[35] For air, the value of C_g is set to 7.6×10^{-5} m-K/N.[64]

The size-dependent thermal conductivity predicted by the Holland model comes from the dependence of the boundary scattering term on L. In addition to their small length

scales, periodic nanostructures in np-Si may also impede thermal transport by acting as phononic crystals. Phononic crystals are the acoustic wave equivalent of photonic crystals, where a periodic array of scattering sites within a homogenous host material prevents certain acoustic frequencies from existing in the crystal.[65] The modified DOS can be calculated by solving for the eigenmodes of an infinite 2D crystal structure[66] and integrating the number of modes with respect to frequency for all directions in the first 2D Brillouin zone.[67] Once calculated, the modified DOS can be substituted into Equation 12 to solve for thermal conductivity. Hopkins et al. demonstrated a plane-wave expansion (PWE) technique[66] that can be implemented within the Holland model to account for phononic crystal effects in periodically nanostructured silicon.[67]

Phonon scattering is the primary mechanism for thermal conductivity reduction, but a growing body of research has suggested that ultrasonic attenuation (Akhieser damping) play a significant role in the attenuation of low-energy phonons.[68-74] Akhieser damping occurs when acoustic phonons disturb the occupational states of thermal phonons, whose frequencies depend on the strain in the lattice. The disturbed thermal phonons collide with one another, returning the system to equilibrium as energy is removed from the acoustic wave.[69] The attenuation coefficient is formulated as

$$\alpha = \frac{CT}{2\rho v^3}\frac{\omega^2\tau}{1+\omega^2\tau^2}\left(\langle\gamma^2\rangle - \langle\gamma\rangle^2\right) \tag{14}$$

where C is the volumetric heat capacity, ρ is the density, v is the acoustic phonon velocity, and γ is the Grüneisen parameter.[68, 75, 76] Although Akhieser damping is not strictly a

scattering process, it can be crudely approximated as such by adding an extra scattering rate to Equation 11

$$\tau_A = \tau_{inf}\left(1+\frac{1}{\tau_{th}^2\omega^2}\right) \tag{15}$$

where τ_A is the relaxation time contribution due to Akhieser damping[69], τ_{inf} and τ_{th} are fitting parameters obtained by comparison to experimental data of phonon lifetime at low frequency (< 1 THz).[77, 78] For silicon at T = 300 K, the fitting procedure yields values of τ_{inf} = 5 ns and 28 ns for the longitudinal and transverse branches, respectively, and τ_{inf} = 14 ps for both branches.[32]

Solutions to the BTE under the relaxation time approximation have advanced understanding of phonon transport. However, this approach relies on using fitting parameters to match existing experimental data and could therefore limit predictive capability. Advances in computing have enabled a multitude of novel approaches based on atomic simulations.[33, 59, 79, 80] Broido et al.[81] estimated the temperature-dependent thermal conductivity of silicon using a first-principles theoretical approach that implements an exact solution to the BTE using only the interatomic force constants from density functional theory.[82] Esfarjani et al. used a similar approach and performed a modal decomposition of the thermal conductivity to obtain a MFP accumulation function for silicon at room temperature.[34] Henry et al. implemented a Green-Kubo approach to calculating thermal conductivity[83, 84] and performed a modal analysis to derive an expression for thermal conductivity with respect to phonon frequency and polarization.[32] A compilation of the various MFP accumulation functions obtained by these techniques is

shown in Figure 6. The MFP accumulation function generated from the Holland model deviates from that of the computation models, but the ability to incorporate impurity scattering, Akhieser damping, and phononic crystal effects without lengthy computational times makes it useful for this work.

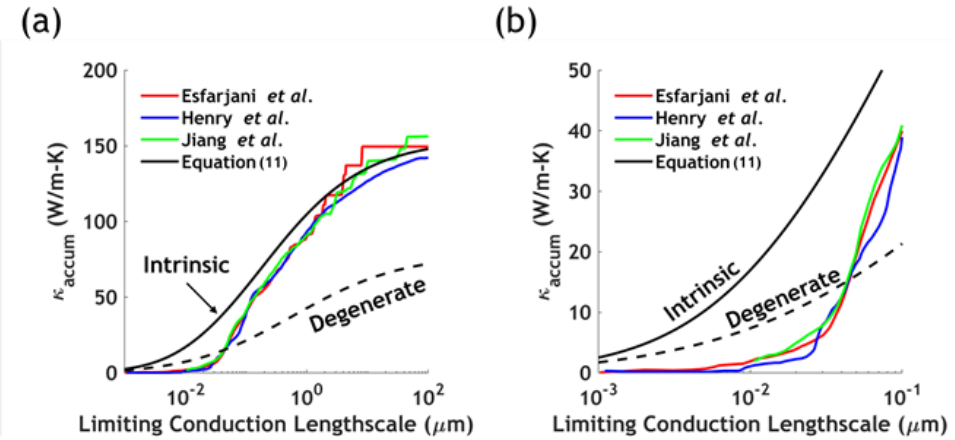

Figure 6 - (a) Silicon thermal conductivity accumulation functions, generated using Equation 12, for both intrinsic (un-doped) and degenerate ($n=7x10^{19}$ cm^{-3}) cases. Additional accumulation functions are used for qualitative comparison with existing literature values.

CHAPTER 3. DEVELOPMENT OF NANOSTRUCTURED POROUS SILICON FOR THERMOELECTRIC APPLICATIONS

3.1 Fabrication Process

The np-Si samples were prepared by Silniva Corporation, where the general procedures is categorized by three stages: (1) the production of micron-sized doped silicon powders from bulk crystalline silicon using high energy ball milling,[85, 86] (2) the formation of a green (non-sintered) pellet from the milled powder, and (3) the sintering and metallization of the compacted pellet to produce bulk-nanostructured porous silicon.

3.1.1 Milling Bulk Powder to Control Particle Size

Bulk powders (125 - 500 μm) of polycrystalline doped silicon were used as source materials and separate mills were used for the n-type and p-type powders to avoid cross-contamination. The milling time was the primary process variable, and times between 20 minutes and 945 minutes were used to obtain controlled particle sizes distributions (PSD). The batches were separated into “coarse” (3.5 μm), “fine” (1.05 μm), and “super-fine” particles (0.32 μm); detailed PSD measurement results are shown in Figure 7. The particle size of the milled powder was quantitatively characterized using a Microtrac X100 laser diffraction (LD) system. LD measurements use the theory of Fraunhofer diffraction, which states that the intensity of scattered light is directly proportional to the particle size, to calculate the PSD by approximating the particles as spheres.[87, 88] The true shape of milled silicon is irregular, but Naito et al., found the spherical approximation to yield results within 10% of the true PSD for micron-sized boron nitride powder exhibiting

similar geometries to the silicon powder used in this work.[89] Based on these observations, the approximation of the particles as spheres is not considered to be a significant source of uncertainty in the PSD measurement results.

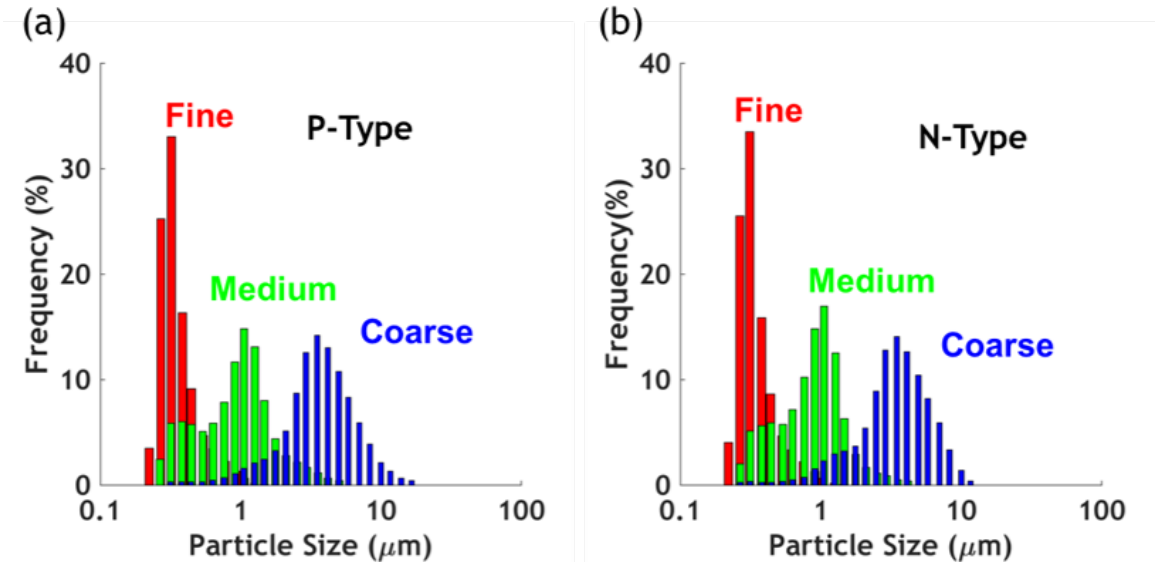

Figure 7 - Particle size distribution before sintering for (a) p-type powder and (b) n-type powder. The reported diameters for each powder is given as the peak in the histogram for each distribution. The characteristic diameters are 3.5 µm (coarse), 1.05 µm (medium), and 0.32 µm (fine) for both p-type and n-type powder.

3.1.2 Formation of Green Pellets

Once the powder is milled to a desirable particle size, a green compact is formed by mixing the powder into a binding matrix and pressing the mixture into a compact pellet. An ideal binding matrix should provide mechanical robustness and act as a lubricant between silicon particles during compaction, thereby enabling their reorientation into a close-packed structure.[90] A total of 119 combinations of binders and solvents were tested, and a slurry composed of acetone (technical grade) and polyvinyl butyral (Mowital B 60HH, 13.44 wt. %) was chosen based on a qualitative assessment of the mechanical

properties of the green pellets. The mixed slurry was dried in ambient conditions and compacted at 270 MPa in an overhead die press to form the green pellet.

3.1.3 Sintering and Metallization

The green pellet contains a percolated network of silicon particles with point contacts between adjacent particles. A sintering process is implemented to grow these point contacts into solid "necks" through the self-diffusion of silicon at elevated temperatures.[91] The self-diffusion of silicon towards the contact points is driven by the reduction in free energy as solid-vapor interfaces are replaced with solid-solid interfaces.[92-94] The rate of neck growth and densification of the powder compact can be controlled via sintering time, temperature, particle geometry, and surrounding gaseous environment.[93] A well-designed sintering process would result in necks that are large enough to exhibit the electronic properties of bulk degenerate silicon, but small enough to inhibit phononic conduction between particles (see Figure 6).

In a seminal paper on sintering kinetics, Ashby considered six distinct diffusion mechanisms that led to neck growth during sintering and identified three stages of sintering: (1) an initial growth stage where particles are distinguishable, (2) an intermediate densification stage where the porosity transitions from open to closed, and (3) a final densification stage where the porosity is eliminated and the bulk density is recovered.[92] Whereas previous efforts at bulk nanostructuring in silicon for TE applications have focused on sintering until the third and final stage,[27, 31] this work limited sintering to the initial stage and achieved neck sizes of ~20-50 nm.[65, 66] Previous studies on c-Si, compiled in Figure 6, indicate that necks of this size should significantly reduce the

phononic contribution to the thermal conductivity but should have minimal impact on the electrical conductivity.[12, 32, 34, 46, 95]

Lebrun et al. applied Ashby's formulations to silicon powder and experimentally demonstrated that vapor transport of silicon monoxide from the particle surface to the neck is the dominant growth mechanism for micron-sized silicon particles covered by an oxide layer.[93] Under these conditions, the neck growth rate is given by[92]

$$\frac{dx}{dt} = P_v \left(\frac{\gamma_s \Omega}{kT} \right) \left(\frac{\Omega}{2\pi\rho kT} \right)^{\frac{1}{2}} K, \tag{16}$$

where $\frac{dx}{dt}$ is the neck radius growth rate, P_v is the vapor pressure of SiO, γ_s is the surface free energy, Ω is the atomic volume, and K is the curvature at the neck defined by[96]

$$K = \left(\frac{2(a-x)}{x^2} - \frac{1}{x} \right) + \frac{2}{a}, \tag{17}$$

where a is the particle radius. Equation 16 can be numerically integrated to determine the relationship between sintering temperature, sintering time, and neck diameter. The results are plotted in Figure 8.

The vapor transport model predicts that, when the pellet is suddenly brought to its sintering temperature, the neck will experience an initial period of rapid growth before stabilizing. The early growth is driven by the fact that $K \propto x^{-1}$, and substituting Equation 17 into Equation 16 yields $\frac{dx}{dt} \propto x^{-1}$. After the initial period of rapid neck growth, the neck

growth rates converge and the neck size stabilizes at a value determined primarily by the temperature-dependent vapor pressure

$$P_v = P_o exp\left(\frac{-Q_{vap}}{k_b T}\right), \tag{18}$$

where P_o is a pre-exponential factor from experimental data and Q_{vap} is the heat of vaporization.

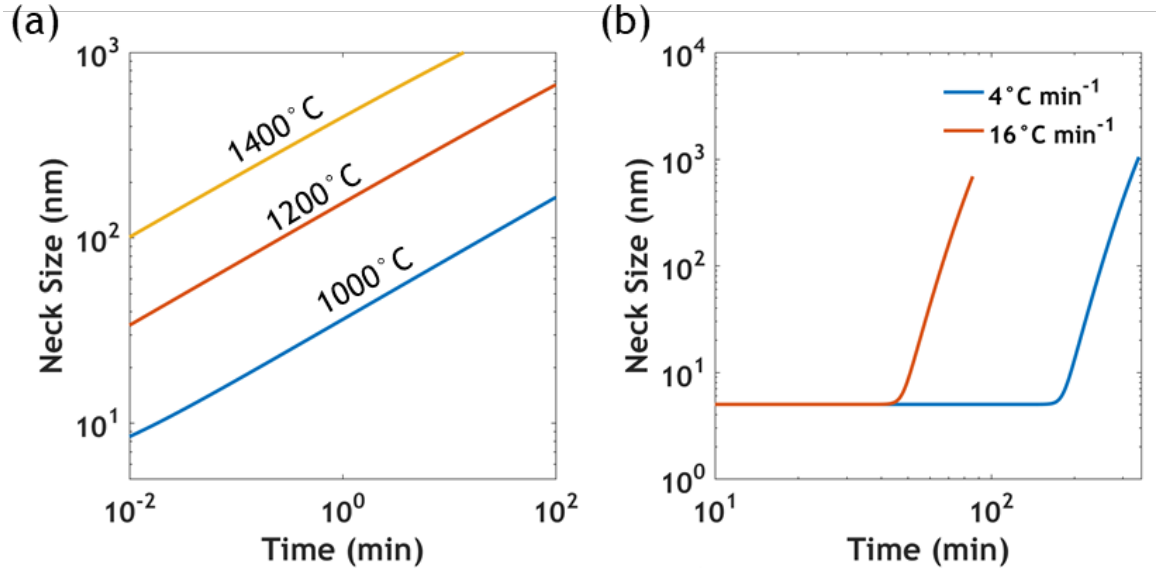

Figure 8 - (a) Neck diameter as a function of time spent at final sintering temperature, according to Equation 16. Initial neck growth is nearly instantaneous, due to the high curvature of small necks, but stabilizes as the curvature of the neck decreases with size. (b) Transient neck growth at 1400°C for temperature ramp rates of 4°C min^{-1} and 16°C min^{-1}.

For practical purposes, a slow ramp rate from room temperature must be used to avoid the development of thermal stress that could potentially cause warping and breakage in the green pellet. Figure 8(b) shows the transient neck size during the ramping process. At 16°C min^{-1}, negligible neck growth is expected for the first 40 minutes and the neck

will not reach a diameter of 50 nm until after 58 minutes. By the time the pellet reaches 1400°C, the neck will have grown to 600 nm at which point vapor transport is no longer the dominant sintering mechanism. At 4°C min^{-1}, the onset of neck growth occurs after 3 hours and reaches 50 nm after 4 hours. The discrepancy between the growths rates in Figure 8(a) and (b) demonstrate that, for necks on the order of 20-50 nm, the required sintering time is driven by the temperature ramp rate rather than the final sintering temperature. Once the sintering process is carried out, the pellets were cooled at 4 °C min^{-1} to minimize thermal stresses.

Upon completion of the sintering process, the pellets are metallized for property measurements. The metallization was performed using a Unisonik-MD ultrasonic solder gun and S-Bond® 220M solder. Alternative metallization techniques (*e.g.* silver paste, electroplating, gold leaf, etc.) were also tested, but ultrasonic soldering was chosen based on its superior bond with silicon and ease-of-use.

3.2 Experimental Property Measurements

The np-Si samples were characterized through experimental measurements of their effective thermoelectric properties: thermal conductivity (κ_{eff}), electrical conductivity (σ_{eff}), and Seebeck coefficient (S_{eff}). The effective TE properties were measured on two p-type samples and two n-type samples. These pellets were randomly chosen from batches containing six samples each, and the remainder of each batch was used for destructive material characterization (*e.g.*, atom probe tomography). The measurement results at standard atmospheric pressure are displayed in Table 2.

Table 2 - Effective electrical and thermal properties of np-Si samples at standard atmospheric pressure.

Sample	κ_{eff} (W/m-K)	σ_{eff} (kS/m)	S_{eff} (μV/K)	ε
p-type, sample 1	1.1 ± 0.1	25.1 ± 2.6	+173 ± 19	0.36
p-type, sample 2	1.1 ± 0.1	26.5 ± 2.6	+178 ± 19	0.35
n-type, sample 1	1.0 ± 0.1	18.7 ± 1.5	-180 ± 20	0.36
n-type, sample 2	1.0 ± 0.1	18.9 ± 1.5	-181 ± 20	0.35

3.2.1 Electrical Property Measurements

The measurements of σ_{eff} were performed according to the ASTM B193-16 standard.[97] This standard involves independent measurement of the electrical resistance (R) and the dimensions of the pellet. These measurements are then used to calculate the effective electrical conductivity $\sigma_{eff} = t/RA_c$ where t is the thickness of the pellet and A_c is the cross-sectional area. The measurement of S_{eff} was performed according to the direct method within ASTM E977-05.[98] In this standard, a known temperature difference (ΔT) is imposed on the sample and the output Seebeck voltage is compared to a calibrated reference sample to calculate the sample's Seebeck coefficient. The temperature gradient was imposed in the same orientation as the measurement of σ_{eff} to eliminate errors due to anisotropy in the sample. The calibration measurement was performed on a constantan sample ($S \approx 35$ μV/K)[99] and the contribution from the leads ($S_{leads} \approx 1.5$ μV/K) was found to be negligible compared to the measured values of S_{eff} for np-Si. All measurements were made with $\Delta T < 20$ K and centered about T=300 K to minimize the impact of temperature-dependence on measurements of S_{eff}.

3.2.2 Thermal Property Measurements

Measurements of κ_{eff} were made using a transient plane source (TPS) technique (commercial name: Hot Disk® TPS 2500 S). The TPS sensor, shown in Figure 9, consists of a nickel spiral pattern surrounded by polyamide for electrical insulation. During the measurement, direct electrical current is sourced through the sensor's nickel spiral pattern and the generated Joule heat is conducted into the sample. The voltage drop across the sensor is measured simultaneously, and the transient resistance of the sensor is used to calculate the temperature response of the sensor during the measurement. The transient temperature response of the sensor is fit to an analytical solution to obtain the sample's volumetric heat capacity and thermal conductivity from a single measurement.[100]

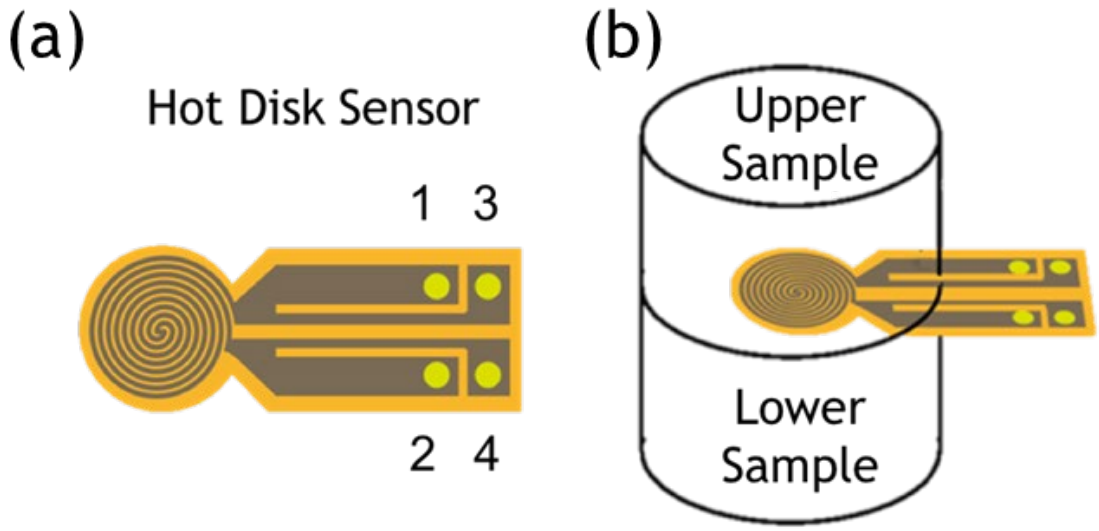

Figure 9 - (a) Diagram of Hot Disk sensor. A nickel spiral pattern is encased in a thin layer of polyamide tape for electrical insulation. Electrical current is sourced from lead 1 to lead 2 and causes Joule heating in the spiral pattern. The voltage between lead 3 and lead 4 is simultaneously measured and used to calculate the temperature-dependent resistance of the nickel spiral. (b) A typical Hot Disk measurement places the sensor between two identical samples.

The analytical solution relies on two critical assumptions: (1) the thermal waves do not reach the sample boundaries (i.e. the sample can modeled as a semi-infinite solid), and (2) the temperature rise of the sensor is small ($\Delta T < 10$ K) such that the relationship between temperature and resistance can be considered linear. The proper selection of measurement time, sensor radius, and heating power is critical towards ensuring the validity of these assumptions. The probing depth of the thermal wave is formulated as

$$\Delta_p = 2\sqrt{D * t_m}\,, \tag{19}$$

where D is the thermal diffusivity of the sample and t_m is the measurement time. In order to satisfy the first assumption, the sensor radius and measurement time should be chosen such that Δ_p is smaller than the shortest distance from the sensor to the sample boundary. Furthermore, the measurement's sensitivity to the thermal diffusivity of the sample is maximized at some characteristic time

$$t_{char} = \frac{r^2}{D}, \tag{20}$$

where t_{char} is the characteristic time and r is the sensor radius. When the measurement time and characteristic time are matched, the probing depth can be found by substituting Equation 20 into Equation 19 to obtain

$$\Delta_{p,char} = 2r\,. \tag{21}$$

Therefore, the sensor radius should be selected such that the minimum distance between the sensor and sample boundary is equal to the sensor diameter, and the appropriate

measurement time can be estimated by using an approximate diffusivity value in Equation 20. The heating power is selected such that the sensor's temperature rise is between 1 K and 10 K during the measurement.

In porous samples, both the solid matrix and the gaseous pores contribute to the effective thermal conductivity. The ability to measure the thermal conductivity of porous samples at reduced pressures (~ 1 Pa) could provide insights on the relative magnitudes of these contributions and allow for the solid matrix to be independently characterized. However, the interface between the sensor and sample could become a dominant thermal resistance at low pressure and affect the measurement's accuracy. A series of pressure-dependent measurements were performed on calibrated samples to determine: (1) if the contact resistance between the sensor and sample could affect the accuracy of the measurement at low pressure, (2) if the effects of contact resistance could be mitigated by polishing the samples, and (3) if the use of thermal grease between the sensor and sample would adversely affect the accuracy of the measurement due to the relatively high thermal conductivity of the thermal grease ($\kappa \approx 8$ W/m-K).

The impact of an elevated contact resistance at low pressure was characterized by measuring a reference standard of stainless steel 304 (NPL 2S09, $\kappa = 14.3 \pm 0.5$ W/m-K) in ambient conditions and at a reduced pressure of ~1 Pa. The reference material is not porous, so any deviation at reduced the pressure indicates that the increase in contact resistance affects the accuracy of the low-pressure measurement. The transient temperature response and thermal conductivity measurement values are shown in Figure 10.

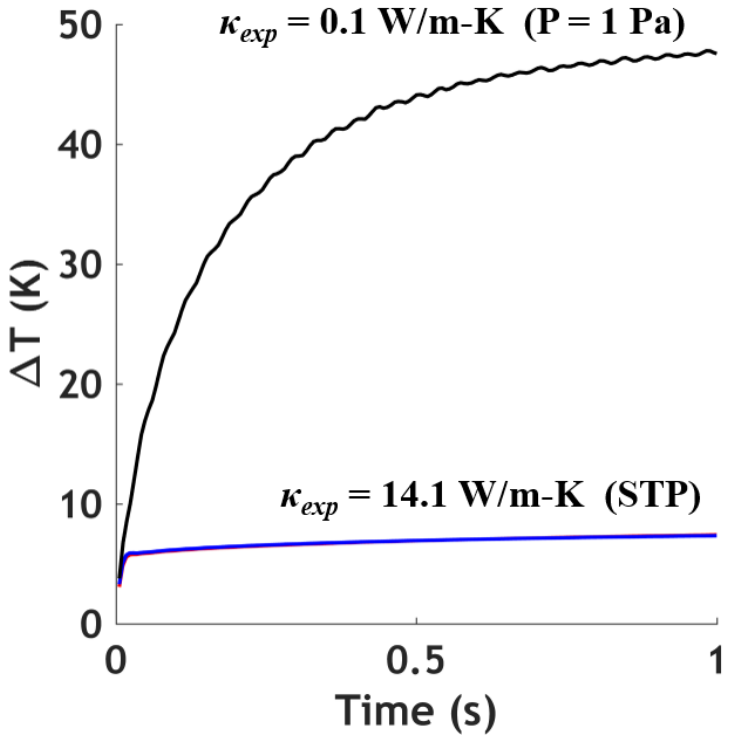

Figure 10 - Transient temperature response of stainless steel 304 at ambient conditions (red and blue) and reduced pressure (black). Heating power, measurement time, and sensor radius were kept constant across all measurements. The large temperature rise of the sensor at reduced pressure indicates that the elevated contact resistance prevents the flow of heat from the sensor into the sample. Measured values of thermal conductivity agree with reference values at ambient conditions but deviate by two orders of magnitude at reduced pressure, indicating that the elevated contact resistance affects measurement accuracy.

The results in Figure 10 indicate that the large contact resistance at low pressure prevents the flow of heat from the sensor into the sample, and therefore causes an artificially reduction in the measured thermal conductivity. Mechanically polishing the sample could reduce the contact resistance and restore the accuracy of the measurement at low pressure. The sufficiency of this solution was tested by measuring a fused silica mirror substrate (Thorlabs PF10-03, κ = 1.4 W/m-K).[101] A surface quality of 40-20 scratch-dig and a surface flatness of $\lambda/10$ were specified by the manufacturer, therefore these substrates

were assumed to represent an upper limit on what could be achieved by mechanical polishing.[102] The measurement results are shown in Figure 11. As was the case with stainless steel, the temperature rise was significantly larger at reduced pressure despite the high surface quality of the fused silica sample. Therefore, it can be concluded that the reduction in contact resistance due to mechanical polishing would be insufficient to achieve accurate thermal conductivity measurements at low pressure.

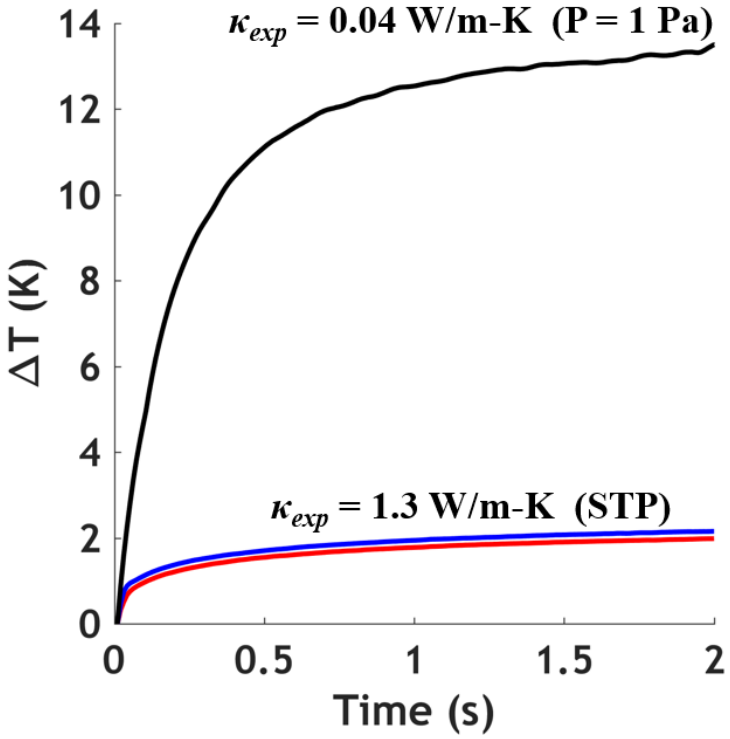

Figure 11 - Transient temperature response of fused silica at ambient conditions (red and blue) and reduced pressure (black). The measurements at ambient could reliably reproduce the literature value of thermal conductivity, but the low-pressure measurement showed similar characteristics to the measurement of stainless steel, indicating that mechanical polishing would be an insufficient solution to the issue of contact resistance.

Thermal grease is another common solution for reducing contact resistance. However, the application of thermal grease between the sensor and sample may adversely

impact the accuracy of the measurements due to the relatively high thermal conductivity of the thermal grease (Arctic Alumina, $\kappa \approx 4$ W/m-K). The impact of thermal grease on contact resistance and measurement accuracy was investigated by measuring fused silica: (1) without thermal grease at ambient pressure, (2) with thermal grease at ambient pressure, and (3) with thermal grease at reduced pressure. The transient temperature data for these measurements are shown in Figure 12. The agreement between the three measurements indicates that the use of thermal grease is effective in reducing the contact resistance at low pressure without otherwise influencing the measurement.

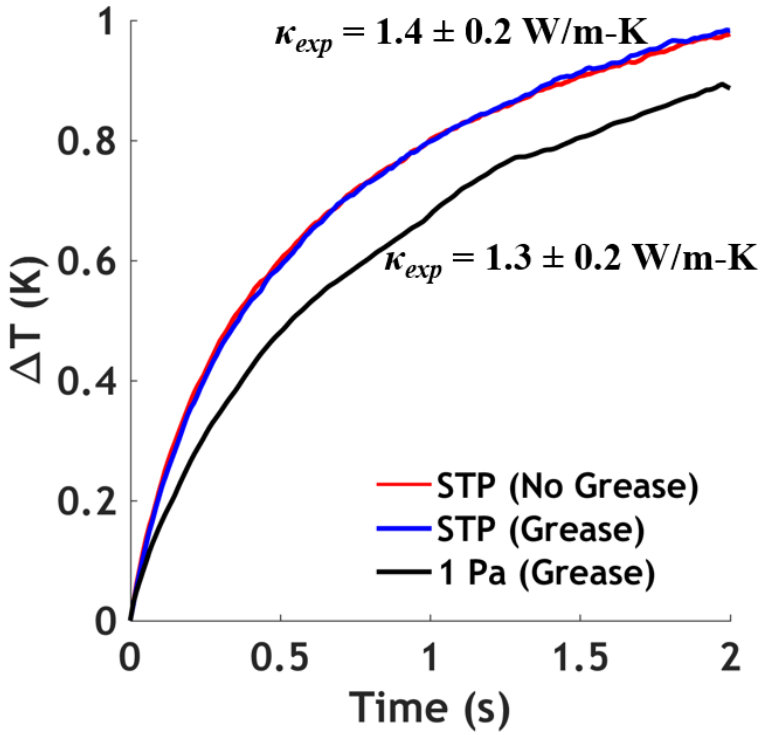

Figure 12 - Transient temperature response of fused silica at ambient pressure without thermal grease (red), with thermal grease (blue), and with thermal grease at reduced pressure (black). The use of thermal grease has negligible impact on the measurement at ambient pressure. The measured thermal conductivity at reduced pressure was within the margin of error of the literature value (1.4 W/m-K).

The effective thermal conductivity of the np-Si samples was measured across a range of pressures (1 Pa – 100 kPa). The pressure-dependent thermal conductivity measurements are shown in Figure 13.

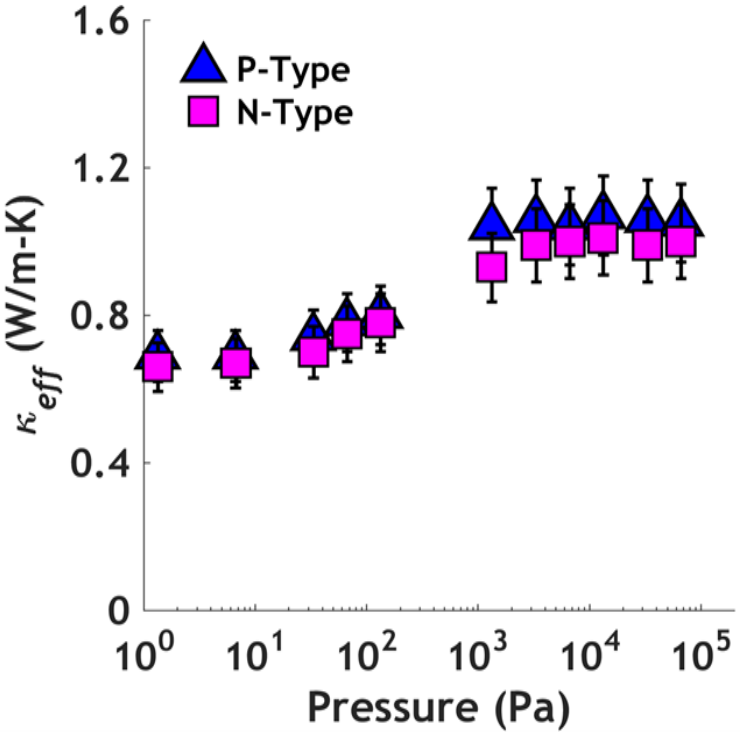

Figure 13 - Pressure-dependent thermal conductivity of np-Si for both p-type and n-type at room temperature. Evacuation of the gaseous pores resulted in a 30% decrease in effective conductivity of np-Si.

3.3 Material Characterization Results

One of the key questions in this work relates to the consistency between the effective TE property measurements of np-Si and the model of phonon transport in c-Si under the relaxation-time approximation. To address this question, it is critical to understand the microstructural and compositional properties of the np-Si samples. To that end, the composition and structure of the np-Si samples were characterized using PSD

measurements, atom probe tomography (APT), and SEM imaging. The characterization results were incorporated into a numerical model for comparison with the experimental TE property measurements.

3.3.1 Atom Probe Tomography Measurements

Atom probe tomography (APT) measurements were performed to examine the spatial concentration of dopant atoms after the sintering process. The results and analysis for the APT measurement, presented in Figure 14, show a non-uniform distribution of dopant atoms in both the p-type and n-type samples. Transmission electron backscatter diffraction was used to identify the regions of elevated dopant concentration as grain boundaries. The observed segregation of dopant atoms towards grain boundaries is consistent with previous literature and attributed to the rapid diffusion of impurities within grain boundaries.[103, 104] A second APT measurement was performed far from a grain boundary to establish a bulk dopant concentration of $n = 10^{20}$ atoms·cm^{-3} for the n-type samples and $n = 7\text{x}10^{19}$ atoms·cm^{-3} for the p-type samples.

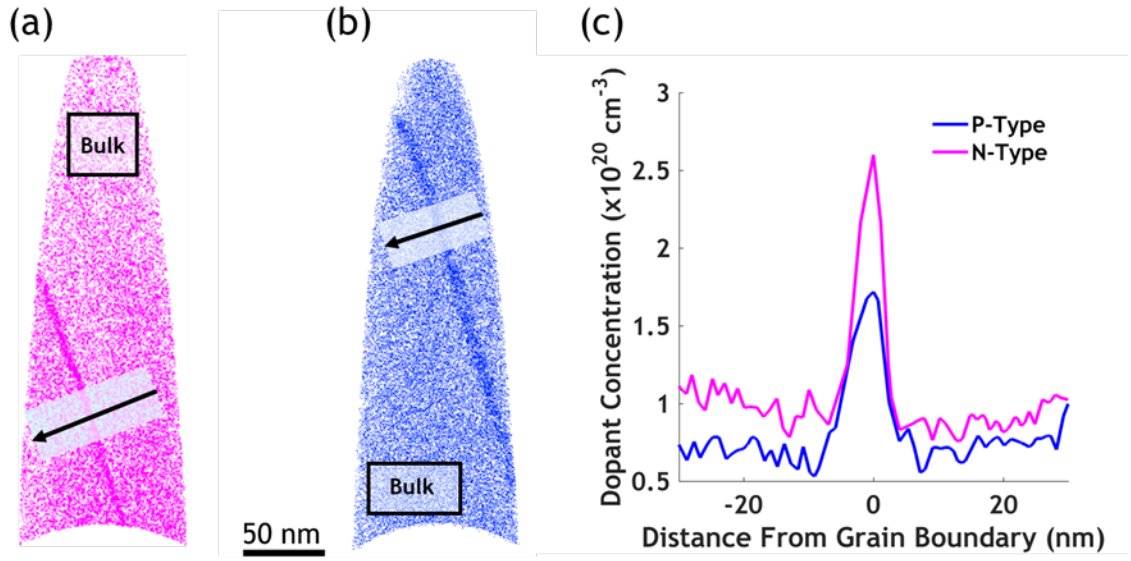

Figure 14 - Atom probe tomography shows variation in the concentrations of dopant atoms near grain boundaries for both (a) n-type (purple) and (b) p-type (blue). The bulk dopant concentration was established by analyzing a region far from the grain boundary (bulk). (c) Dopant concentration profiles for both dopants are plotted with respect to distance from the grain boundary.

3.3.2 Scanning Electron Microscopy

The structure of the sintered np-Si samples was examined using a scanning electron microscope (SEM). The resulting images, shown in Figure 15, provide qualitative information about: (i) the PSD after sintering, (ii) the size of the necks between adjacent particles, and (iii) the degree of compaction between particles. The particles in Figure 15(a) can be distinguished from one another, giving qualitative confirmation that the sintering process did not progress past the initial stage described by Ashby.[92] Adjacent particles appear to be connected through solid necks with limiting dimensions on the order of 10-100 nm, which is desirable for the selective reduction of thermal conductivity in c-Si (see Figure 6). The magnification of the SEM image in Figure 15(b) is insufficient to provide information about the neck size, but the observed particles appear to be in qualitative

agreement with the PSD measurement of 3.5 µm. Furthermore, the arrangement of particles in both images gives qualitative confirmation of the densely-packed structure of the np-Si samples.

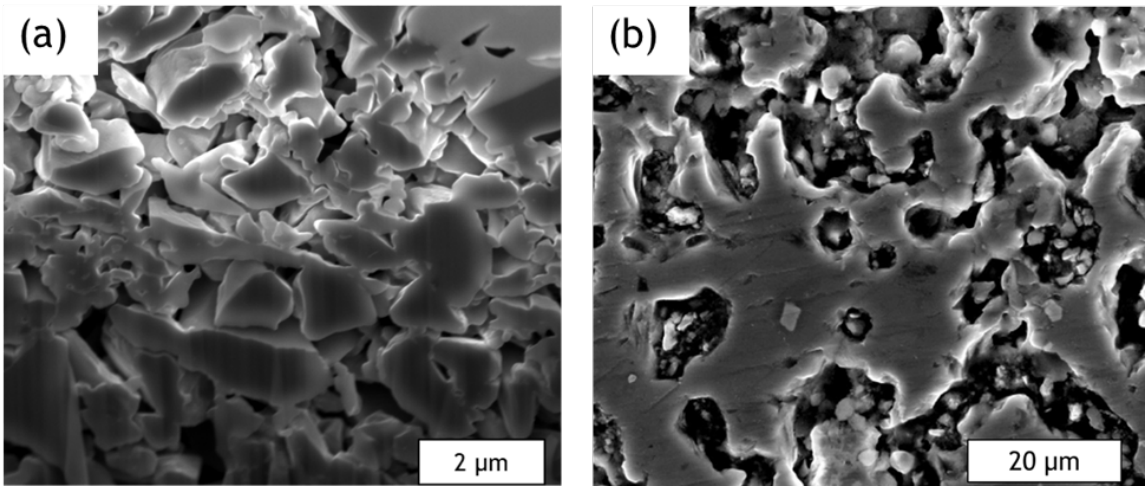

Figure 15 - (a) SEM image of a sintered n-type sample and (b) SEM image of the n-type sample used for APT analysis. The large continuous regions were created during the sample preparation for APT measurement and are not present in typical np-Si samples. P-type and n-type samples appear identical.

3.4 Numerical Modeling

In an attempt to explain the experimentally observed low thermal conductivity, a numerical model was created to examine the consistency between the experimental measurements, material characterization results, and the thermal conductivity model from Equation 12. The model geometry was based on the sintered-sphere geometry described by Ashby et al., which is defined by two geometric parameters: the diameter of the spherical particles and the diameter of the neck at the interface between spheres.[92] Even though the silicon particles are not perfect spheres, this is a useful simplification that builds

upon the work of others. The sphere diameter is set to a characteristic particle size based on the histogram peak from the PSD measurements (see Figure 7). The diameter of the neck is left as a free parameter for fitting to experimental data. A characteristic neck size for each set of samples was determined by fitting the model results to the experimental measurements of κ_{eff} and σ_{eff}. All length scales in the np-Si samples are assumed to be large enough to avoid electronic size effects, so predictions of σ_{eff} only rely on the model's geometry and the dopant concentration. Therefore, discrepancies between the characteristic neck sizes for κ_{eff} and σ_{eff} point towards an inability of the relaxation-time model from Equation 12 to predict the size-dependent thermal conductivity of c-Si accurately.

3.4.1 Application of Material Characterization Results to Numerical Model

The results from the APT analysis were used to model the spatial distribution of dopants. The surface area of the milled powder is assumed to have a dopant concentration identical to the elevated concentration observed in the grain boundaries of both the n-type and p-type np-Si. This assumption builds on the idea that intergranular fracture is the dominant fracture mechanism during the milling of silicon powder near room temperature.[105] Since the powder size is reduced by several orders of magnitude during the milling process, we assume that all free surfaces of the np-Si were once grain boundaries in the coarse powder. Therefore, the surface area of the milled powder is assumed to have a similar doping concentration to the grain boundary measured by APT analysis (see Figure 14), and this concentration profile is applied to the interfacial region between the particles. The dopant concentration in the rest of the sphere was set to the bulk dopant concentration obtained from APT analysis.

Once the model geometry and dopant concentration profiles are established, the spatially-dependent thermal conductivity of the silicon, $\kappa(z)$, can be obtained using Equations 11 and 12. The scattering rates in Equation 11 are determined by setting $L=d(z)$ and setting $A_1(z)$ using the fitting parameter described in Section 2.2. The thermal conductivity of the gaseous pores is calculated by setting $d=L_{air}(r)$ in Equation 13. The generalized model geometry is shown in Figure 16 alongside an example of the spatially-variant thermal conductivity from Equation 12 and Equation 13.

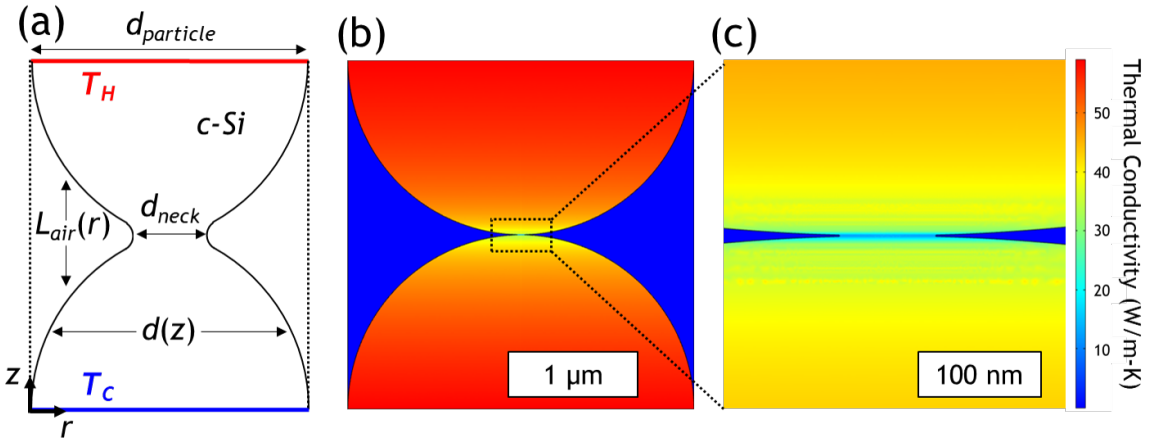

Figure 16 - (a) Geometry and boundary conditions used in the numerical model. Temperature boundary conditions are imposed across the horizontal boundaries of the domain (red and blue lines) and the vertical boundaries (dotted lines) are considered adiabatic. (b) Spatially-dependent thermal conductivity after applying Equations 12 and 13 to the domain. (c) The interfacial region is magnified to show the sharp drop in thermal conductivity at the neck.

The domain shown in Figure 16 represents a unit cell within a packed bed of (spherical) sintered particles. In order to directly compare the results of the numerical model with the experimental results, the np-Si particles are assumed to be packed in a close-random structure as described by Batchelor et al.[106] This assumption is made based on the agreement in porosity between the np-Si samples (~0.35) and the theoretical

porosity of a close-random structure (~0.37).[106] Furthermore, a qualitative assessment of the SEM images in Figure 15 indicates a relatively uniform porosity in the sample, which is characteristic of close-packed structures.[107] The analytical solution by Batchelor et al. for the effective conductivity of packed spheres introduces a scaling factor of

$$\kappa_{eff,random} = 2\kappa_{eff,domain}, \tag{22}$$

where $\kappa_{eff,domain}$ is the effective thermal conductivity of the domain shown in Figure 16 and $\kappa_{eff,random}$ is the effective thermal conductivity of a packed bed in close-random arrangement. Batchelor et al. also considered simple cubic arrays ($\varepsilon = 0.48$) but found the scaling factors to be within 25% of the scaling factor for close-random arrays, despite the large differences in porosity.[106] Therefore, the model results are considered to be insensitive to errors from assuming a close-random packing structure.

The gaseous pores contribute significantly to the experimentally-measured thermal conductivity (see Figure 13) but do not contribute to electrical conductivity, the fitting procedure for thermal conductivity was based on the measurement data at low pressures (1 Pa) to provide a more direct comparison between electrical and thermal transport. The spatially-dependent electrical conductivity within the silicon particles was established by applying literature values for bulk electrical conductivity in silicon (σ_{bulk}) as a function of doping concentration to the dopant concentration established by APT analysis.[55] The use of σ_{bulk} was justified based on the assumption that boundary scattering of electrons is negligible in the np-Si samples due to the small (<8 nm) mean-free-path of electrons in degenerate silicon.[33] The results of the fitting procedure are shown in Figure 17.

3.4.2 Numerical Model Results

The characteristic neck sizes obtained by fitting to thermal conductivity measurements at low pressure are significantly smaller than the neck sizes corresponding to the electrical conductivity measurements. This result suggests that the selective reduction in thermal conductivity is stronger than predicted by the thermal conductivity model used in this work, which is consistent with the discrepancy between the thermal conductivity accumulation functions shown in Figure 6, where the analytical model in Equation 12 over-predicts the thermal conductivity at small length scales compared to atomistic simulations. The inclusion of Akhieser damping in the thermal conductivity model (red line in Figure 17) did not make a significant difference in the predicted value of κ_{eff}. This result is expected because Akhieser damping primarily affects low-frequency phonons (< 100 GHz) but Hopkins et al. demonstrated that high-frequency phonons are the primary contributors to thermal conductivity in nanostructured c-Si.[12]

While the model by Holland et al. has been successfully used for many applications, it is based on a simplified view of thermal transport that may become less applicable at the small length scales of np-Si.[108] More advanced methods have been developed for predicting lattice thermal conductivity at the nanoscale, but predictions for dopant-dependent thermal conductivity in silicon are not yet available in literature.[32, 34, 71, 109] The application of atomistic simulations to studying np-Si would be quite relevant for a future study.

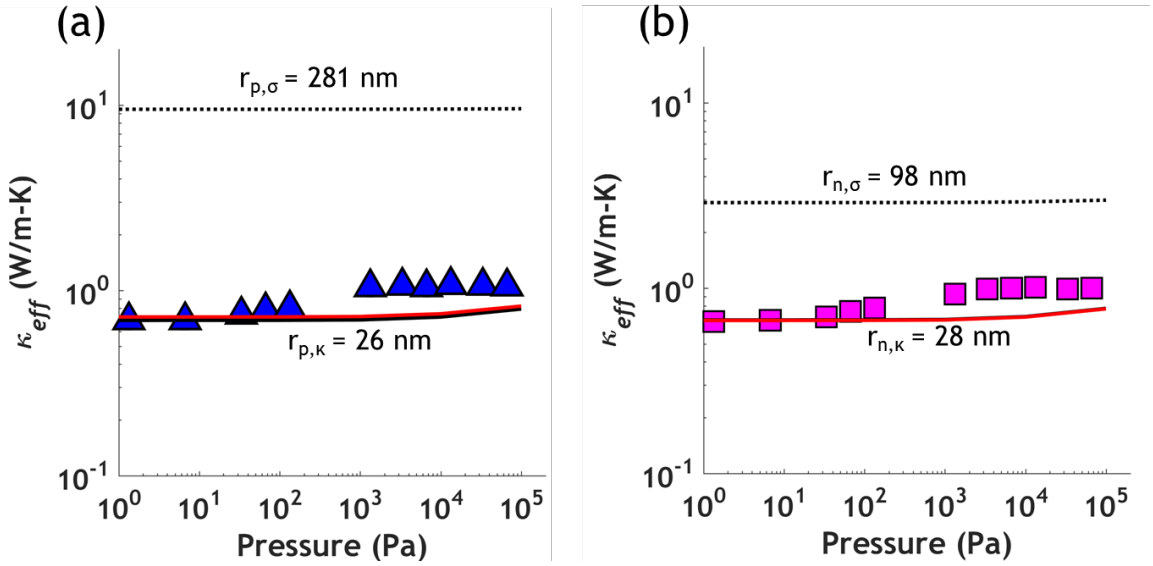

Figure 17 - (a) Fitting numerical model to p-type experimental data at low pressure (blue triangles) yields characteristic neck sizes of 26 nm for thermal conductivity (solid black line). Fitting to electrical conductivity yields a neck size of 281 nm (dotted line). The inclusion of Akhieser damping was not found to make a significant difference in the prediction of κ_{eff} (solid red line). (b) Fitting numerical model to the n-type experimental data at low pressure (magenta squares) yields characteristic neck sizes of 28 nm for thermal conductivity and 98 nm for electrical conductivity. The numerical model under predicts the contribution of air to κ_{eff} at high pressure for both p-type and n-type.

Another explanation for the selective thermal conductivity reduction could be the existence of scattering mechanisms that are not accounted for in the numerical model. Bux et al. observed a reduction in the electron mobility of np-Si as milling intensity was increased and attributed it to the formation of nanocrystals and extended defects during the milling process.[27] The reduction in electron mobility was observed at every level of milling intensity, suggesting the formation of scattering sites with dimensions on the order of the electron MFP (~8 nm) could occur even at early stages in the milling process. These scattering sites are not accounted for in the numerical model and may explain the strong reduction in thermal conductivity.

In addition to the selective reduction of thermal conductivity, the numerical model predicts very little dependence on pressure whereas the experimental results show the gaseous pores accounting for over 30% of the effective thermal conductivity at standard atmospheric pressure. A potential explanation for the strong dependence on pressure is the roughness of the silicon particles, which is not accounted for in the numerical model. Experimental measurements by Buonanno et al.[110] and analytical modeling by Bahrami et al.[111] both observe a significant pressure-dependent decrease in the effective conductivity of packed beds of steel spheres with roughened surfaces. The rough surfaces of the spheres creates interstitial pockets of gas at the interface between adjacent particles, and the rarefaction of these gas pockets at low pressure causes significant reduction of the effective thermal conductivity, particularly as the particles conductivity increases.[111]

3.4.3 Application of Phononic Crystal Effects

Although the np-Si structure in this work was not ideally periodic, the use of phononic crystal patterning has been demonstrated as a potential avenue for thermal conductivity reduction in nanostructured c-Si.[67] The PWE methodology detailed by Kushwaha et al.[66] was implemented for the characteristic geometries used in Figure 17 to investigate the effect of phononic crystal patterning in np-Si. The modified phononic DOS is shown in Figure 18.

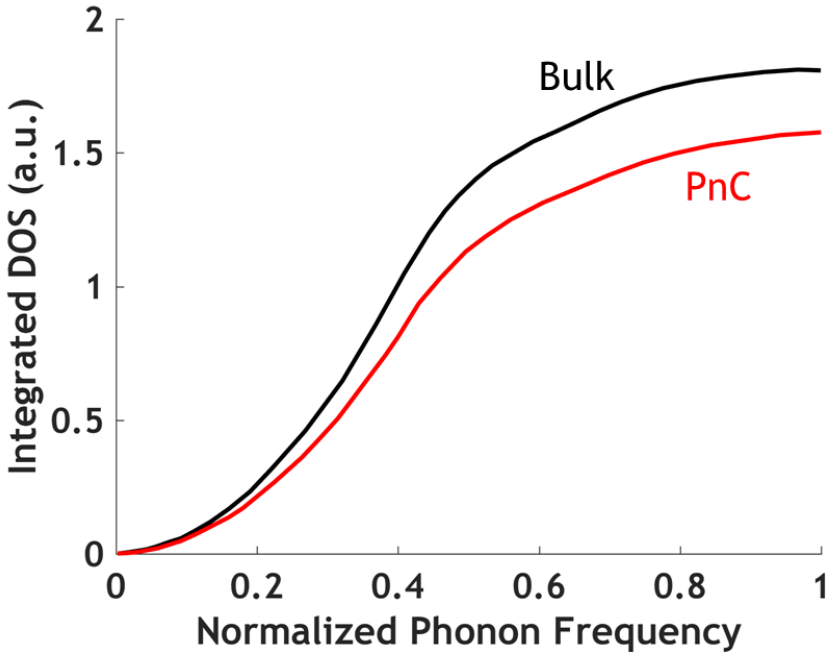

Figure 18 - Reduction in phononic density of states due to phononic crystal effects (PnC). The reduction from the bulk mode density due to PnC can be incorporated into Equation 12 to predict the change in the thermal conductivity accumulation function due to the reduction in phonon mode density.

The impact of phononic crystal patterning on the effective thermal conductivity of np-Si can be observed by incorporating the modified DOS from Figure 18 into Equation 12 to obtain a suppressed thermal conductivity accumulation function, which is then plugged into the numerical model shown in Figure 16. The reduction in κ_{eff}, shown in Figure 19, is ~15% for both the p-type and n-type models. It is worth noting that this reduction is achieved without any optimization of the np-Si geometry to maximize the PnC effects. An optimization study on the geometry of np-Si would be useful towards understanding the full potential of np-Si as a thermoelectric material but is beyond the scope of the present work.

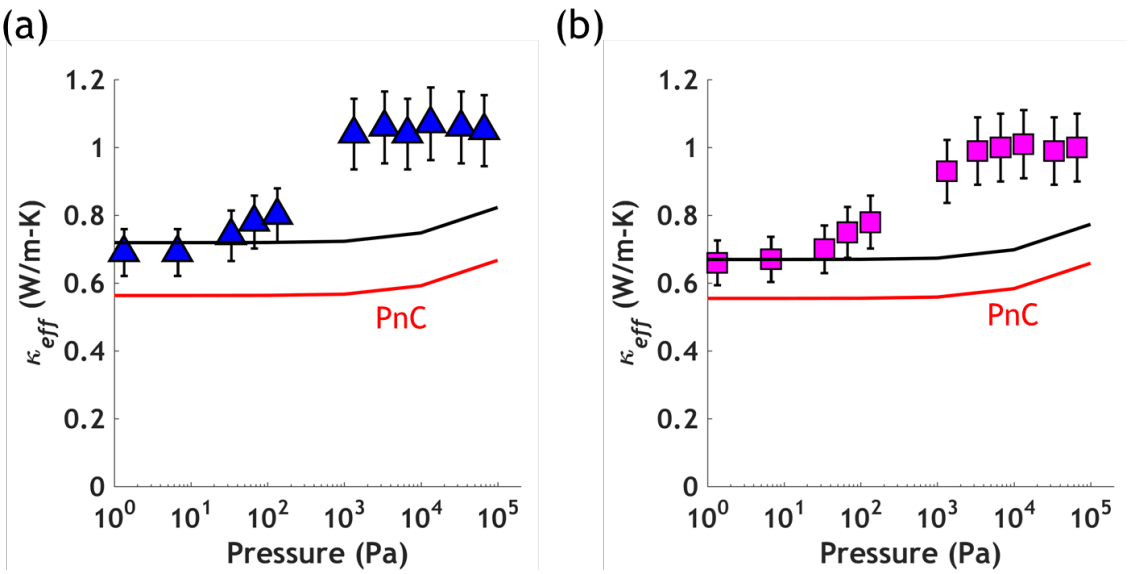

Figure 19 - The incorporation of phononic crystal effects into the numerical model (red line) results in a ~15% reduction in κ_{eff} for both the (a) p-type and (b) n-type models compared to the results obtained from using the bulk mode density (black line).

CHAPTER 4. THERMAL CONDUCTIVITY MEASUREMENTS USING FREQUENCY-DOMAIN THERMOREFLECTANCE

4.1 Traditional FDTR Measurements

4.1.1 Operating Principles of Traditional FDTR

FDTR, which is well described in literature,[37, 39, 45] measures an unknown thermal property, most often thermal conductivity, using a pump-probe laser technique relying on a transducer's temperature dependent thermoreflectance, $R^{-1} \times dR/dT$. FDTR operates by experimentally measuring the phase lag between a periodic heat source and its corresponding surface temperature response as a function of heating frequency. The frequency-dependent phase lag data is fit to an analytical model[40, 112] where the thermal property of interest (most often thermal conductivity) is a free parameter in the analytical model. The value of the fitting parameter that minimizes the mean squared error between the experimental data and analytical model is taken as the measured value.

To absorb the periodic heat source delivered by a laser, FDTR requires the deposition of a thin (~50-100 nm) thermoreflectance transducer atop the sample. An intensity-modulated pump laser (λ_{pump} = 488 nm) is absorbed by the transducer to create a periodic heat source. A probe laser (λ_{probe} = 532 nm) monitors the temperature response of the transducer. Therefore, the transducer serves two purposes: it absorbs the pump beam, which enables isothermal surface heating[45], and it reflects the probe beam, which carries information about the temperature response of the surface to the periodic heat source

encoded by the thermoreflectance of the transducer.[113] Au is the best transducer for the laser wavelengths used in many FDTR setups because the reflectance of Au exhibits a relatively strong temperature dependence at the probe's wavelength of 532 nm, $\left(R^{-1}\times dR/dT\sim 10^{-4}K^{-1}\right)$ and it absorbs well at the pump's wavelengths of 488 nm.[114]

The pump laser's intensity is modulated at a frequency f and creates a temperature oscillation on the sample surface at that same frequency f but with an additional phase-lag θ. The surface temperature oscillation induces a coherent oscillation in the reflectance of the gold transducer. The incoming probe beam is initially at a constant intensity but, upon reflection, becomes modulated at frequency f and picks up the phase-lag θ. The reflected pump and the probe beams take the same path to a photodiode, where their periodic intensities are converted into periodic voltage signals. The individual phases of the voltage signals from the pump and probe are measured as a function of heating frequency. Some small additional phase lag is acquired by the post-sample optics, however, since the reflected paths of the beams are identical, the only source of phase lag between the pump and probe signals arises from the thermal response of the sample and the associated temperature response. Therefore, the phase difference between the pump and probe voltage signals is θ.

An analytical solution to the heat diffusion equation, discussed later in this chapter, can be used to predict θ.[40, 112] The inputs to the model include the thermal conductivity, volumetric heat capacity, and thickness of each layer, the thermal interface conductance between layers, as well as the $1/e^2$ radius of the pump and probe beams. In a typical isotropic sample, the thermal conductivity, κ, and the thermal interface conductance

between the transducer and the sample, G, are unknown. In the case of a multilayered sample, as shown in Figure 20(b-c), the unknown parameters may include: (i) the film conductivity, k_{film}, (ii) the substrate conductivity, k_{sub}, and (iii) the thermal interface conductances, G_1 and G_2. In many multilayer samples, the substrate conductivity is independently measured without the film and κ_{sub} can be treated as a known input parameter to the model. The transducer thickness and thermal conductivity, as well as the volumetric heat capacity of the sample, should be independently measured to minimize the number of unknown variables when fitting. The remaining unknown properties are used as fitting parameters, and the measurement results are the set of fitted values that minimize the mean-squared error between the analytical model and experimental data.

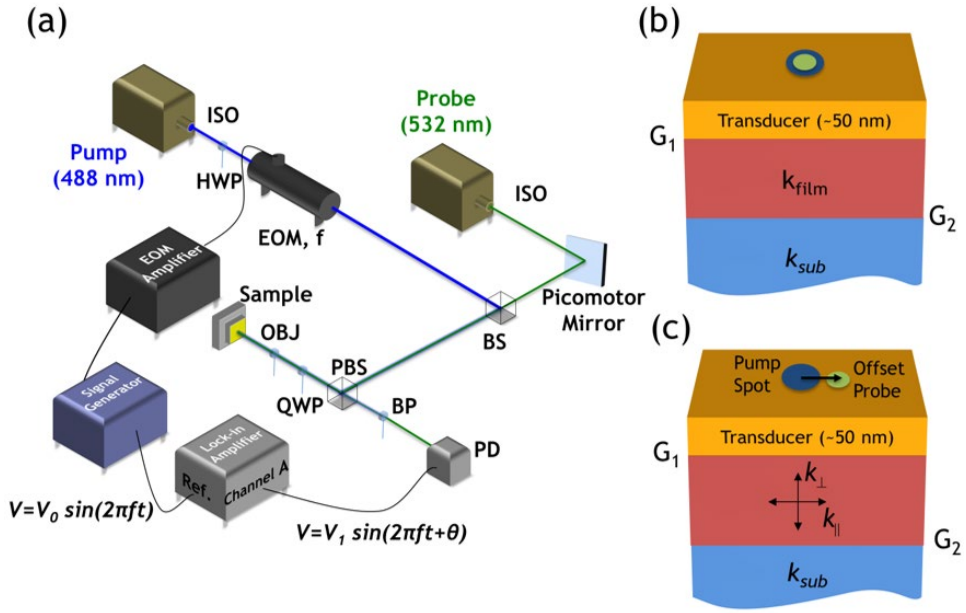

Figure 20 - (a) Schematic of an FDTR set-up. (b) Sample configuration for traditional FDTR on a thin film sample. The pump beam (blue) is concentrically aligned with the probe beam (green). The interfacial thermal conductance between the transducer and film is labeled G_1 and the conductance between the film and substrate is labeled G_2. (c) Sample configuration for offset FDTR. The probe beam is spatially offset from the pump beam using the Picomotor mirror, and the film or

substrate may have unique values for through-plane ($k_{\perp}$) and in-plane ($k_{||}$) thermal conductivity.

4.1.2 Description of Experimental Set-up

The setup used in this work, shown in Figure 20, passes both the pump (Coherent MX-488 SLM) and probe (Coherent Verdi G2) beams through optical isolators (ISO, Conoptics 711A and 711C-3) tuned to their specific wavelengths. The isolators act as optical diodes to prevent light from re-entering and damaging the laser cavities. The signal generator (Rigol DG5252) produces a sinusoidal voltage at a controllable frequency, which is amplified (Conoptics Model 200) to drive the electro-optic modulator (EOM, Model 350-80-01 KD*P Series with reduced aperture). The frequency range of the modulation system is between 9 kHz and 200 MHz. However, we found that the experimental data is most reliable between 400 kHz and 5 MHz. The lower limit of 400 kHz was established to minimize uncertainty due to beam spot size errors and the upper limit was established to avoid high-frequency ambient noise. The EOM is a polarization-dependent optics and must be rotated such that the incoming light is polarized at a 45° angle relative to the EOM's crystal. To more easily achieve this, a half-wave plate (HWP, ThorLabs WPH10M-488) rotates the polarization of the laser before it enters the EOM's aperture and eliminates the need for the user to rotate the EOM thus simplifying the alignment process. The pump and probe beams are co-aligned as they pass through the beam splitter (BS, ThorLabs BS025) and are then directed towards the sample using a polarizing beam splitter (PBS, ThorLabs CM1-PBS251). The beam polarizations are tuned through a quarter-wave plate (QWP, ThorLabs WPQ10M-488) and focused through an objective (OBJ, Nikon MUE31100) onto the sample. The reflected beams are sent to the photodiode (PD,

ThorLabs PDA36A) and their phase-lag relative to the voltage signal generated by the signal generator is measured using a lock-in amplifier (SRS SR844). The phase lag between the two signals, θ, is obtained by independently measuring the phase lag of the reflected beams relative to the signal generator and taking the difference. The individual measurement of the beams is enabled by bandpass filters for each laser respectively (BP, ThorLabs FL488-1 and ThorLabs FL532-10).

4.1.3 Analytical Solution for Traditional FDTR

The analytical solution for traditional FDTR, first presented by Cahill et al.[112], is derived from the frequency-domain solution for periodic point source heating of a semi-infinite solid[115]

$$T(r) = \frac{\exp(-i2\pi fr / D)}{2\pi\kappa r}, \tag{23}$$

where κ is the thermal conductivity of the solid, D is the thermal diffusivity, and r is the radial coordinate. The solution for a Gaussian heat source is obtained by convoluting Equation 23 with the pump's spatial heating profile

$$q_p^{"}(r) = \frac{2A_P}{\pi w_o^{\,2}} \exp(-2r^2 / w_0^2), \tag{24}$$

where w_0 is the $1/e^2$ radius of the pump beam and A_P is the heat absorbed by the transducer. In order to simplify the convolution, Hankel transforms are performed on Equations 23 and 24 to obtain

$$G_q(s) = \frac{1}{\kappa(4\pi^2 s^2 + q^2)}, \tag{25}$$

$$P(s) = A_P \exp(-\pi^2 s^2 w_0^2 / 2). \tag{26}$$

The convolution then becomes the inverse Hankel transform of the product of Equations 25 and 26, which yields the surface temperature

$$\psi(r) = 2\pi \int_0^\infty P_q(s) G_q(s) J_0(2\pi sr) s ds. \tag{27}$$

The reflected probe signal is the weighted average of the surface temperature distribution $\psi(r)$ with the probe's intensity profile acting as the weighting function

$$\Delta T_s = \frac{4}{w_1^2} \int_0^\infty \psi(r) \exp(-2r^2 / w_1^2) r dr, \tag{28}$$

which can be rewritten in terms of a single integral over k that must be evaluated numerically

$$\Delta T_s = 2\pi A \int_0^\infty G_q(s) exp(-\pi^2 s^2 (w_0^2 + w_1^2) s ds). \tag{29}$$

The complex phase of Equation 29 represents the phase lag between the periodic heat source and the surface temperature response is used for comparison with experimental measurements of θ.

4.1.4 Analytical Solution for Multilayer Samples

The solution in Equation 29 can be extended to multilayer geometries using an iterative algorithm first introduced by Feldman.[116] In this method, the layers are numbered sequentially, with $n = 1$ applied to the transducer, and the interfaces are treated as thin layers (~ 1 Å). The only change to Equation 29 is the replacement of $G_q(s)$ with

$$G_q(s) = \left(\frac{B_1^+ + B_1^-}{B_1^+ - B_1^-} \right) \frac{1}{\gamma_1}, \tag{30}$$

and the introduction of an iterative relationship between adjacent layers

$$\begin{pmatrix} B^+ \\ B^- \end{pmatrix}_n = \frac{1}{2\gamma_n} \begin{pmatrix} \exp(-u_n L_n) & 0 \\ 0 & \exp(-u_n L_n) \end{pmatrix} \times \begin{pmatrix} \gamma_n + \gamma_{n+1} & \gamma_n - \gamma_{n+1} \\ \gamma_n - \gamma_{n+1} & \gamma_n + \gamma_{n+1} \end{pmatrix} \begin{pmatrix} B^+ \\ B^- \end{pmatrix}_{n+1}, \tag{31}$$

$$u_n = \left[4\pi^2 s^2 + {q_n}^2 \right]^{1/2}, \tag{32}$$

$${q_n}^2 = \frac{i2\pi f}{D_n}, \tag{33}$$

$$\gamma_n = \kappa_n u_n . \tag{34}$$

Since the substrate is assumed to be infinitely thick ($L >> L_p$), the iterative boundary conditions $B^+ = 0$ and $B^- = 1$ are applied to the final layer. Equation 31 is then iteratively solved until B_1^+ and B_1^- are obtained and used to solve Equation 30, which is then substituted into Equation 29 to obtain θ.

4.1.5 Penetration Depth and Sensitivity Analysis

The periodic heating generates a thermal wave that decays exponentially as it propagates into the sample. The exponential decay length, or thermal penetration depth, is inversely proportional to the heating frequency and is expressed as

$$L_p = \left(\frac{D}{\pi f} \right)^{\frac{1}{2}}. \tag{35}$$

Since FDTR is based on the frequency-domain response of the sample, the measurement is most sensitive to regions where the amplitude of the thermal wave is large. As a result, the heating frequency can be used to control the measurement sensitivity of various parameters of interest. At low frequencies (~100 kHz), L_p is on the order of several microns and the measurement is most sensitive to the thermal properties of the substrate. At higher frequencies (~10 MHz), the penetration depth is commensurate with the thickness of the transducer and the measurement becomes much more sensitive to the properties of the transducer and the thermal interface between the transducer and the substrate. For the case of multilayered samples, the measurement will also show improved sensitivity to the thermal properties of the film.

A quantitative sensitivity analysis can be used to determine the appropriate frequency regimes for the measurement of any sample parameter. The sensitivity of some parameter β is defined as the logarithmic derivative of θ with respect to the system parameter of interest

$$S_\beta = \frac{d \ln \theta}{d \ln \beta} \tag{36}$$

The sensitivity S_β is evaluated numerically by changing the value of β by 1% about the nominal value and observing the corresponding change in the phase of Equation 29. The results of a sensitivity analysis on c-Si are shown in Figure 21 with the nominal parameters listed in Table 3.

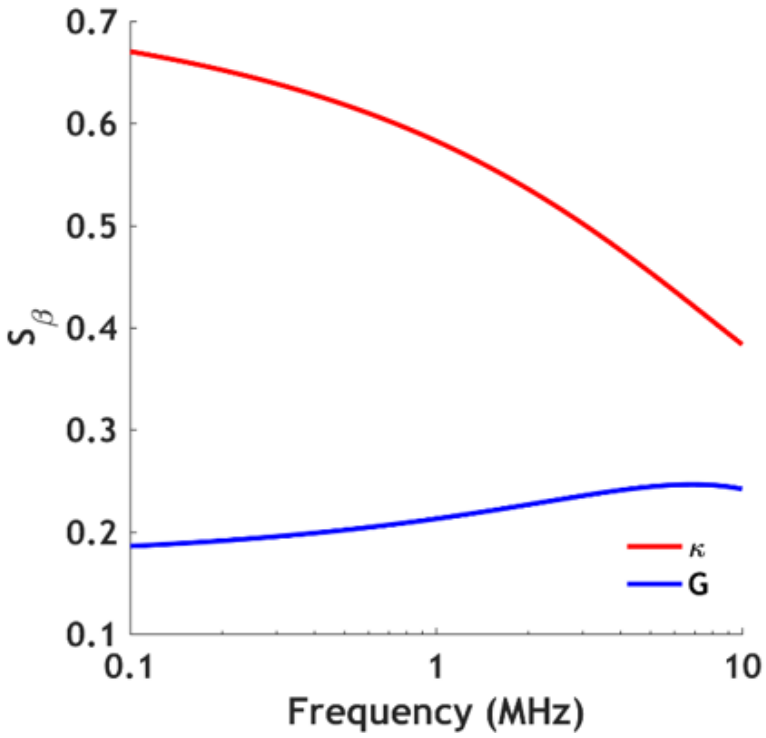

Figure 21 - Sensitivity analysis results for c-Si sample. Higher heating frequencies lead to smaller penetration depths and improved sensitivity to the thermal interface. Lower heating frequencies allow the substrate to dominate the thermal response.

The sensitivity analysis allows one to determine which parameters most heavily influence the measurement response across a range of frequencies. The measurement should be more sensitive to the fitting parameters than the input parameters to prevent small

uncertainties in the independent input measurements from propagating into the final result. This consideration is used to optimize the measurement accuracy by selecting a proper film thickness, transducer thickness, heating frequency range, and spot size. If any input parameter shows greater sensitivity than the fitting parameters, an emphasis is placed on the accuracy of the independent measurement of that input parameter. Input parameters with low sensitivity ($S_\beta < 0.05$) can exhibit relatively large uncertainty ($U_\beta \sim 25\%$) without significantly impacting the uncertainty of the final measurement so long as the sensitivity to the fitting parameters is relatively high ($S_\beta > 0.2$)[117]. In some unavoidable cases, the sensitivity to multiple input parameters may be higher than the sensitivity to the fitting parameters and measurement uncertainty is very high ($U_\beta > 50\%$). For these cases, a robust approach to uncertainty analysis plays a critical role in proper reporting of measurement results.

Table 3 - Nominal parameters for sensitivity analysis shown in Figure 21.

Property	Nominal Value	Uncertainty
$C_{transducer}$	2.5 MJ/m^3-K	5%
$\kappa_{transducer}$	200 W/m-K	5%
$L_{transducer}$	50 nm	3%
r_{probe}	5.0 µm	3%
r_{pump}	5.0 µm	4%
L_{sample}	500 µm	N/A
C_{sample}	1.65 MJ/m^3-K	5%
κ	149 W/m-K	19%
G[45]	200 MW/m^2-K	20%

4.1.6 Uncertainty Estimation for FDTR Measurements

A Monte Carlo computational approach, similar to the methods of other TTR measurements, is used to calculate measurement uncertainty in this work.[118-120] The method used in this work can be categorized into four steps: (1) estimate uncertainty in experimental data and input parameters, (2) generate a new set of input parameters and experimental data based on uncertainty estimations, (3) fit for parameter of interest using generated data and input parameters, and (4) repeat steps 2 and 3 until the set of fitted values converges to a normal distribution. This approach is advantageous because it does not assume a hierarchy of dominant uncertainty sources and incorporates the uncertainty propagations from both the input parameters and experimental noise.

The uncertainty of each input parameter is estimated based on the measurement methodology. Layer thickness, including transducer thickness, was measured using a Tencor P15 profilometer with a spatial resolution of 0.7 Å and a minimum measurable thickness of 10 nm. The uncertainty of thickness measurements was set at 5% based on repeated measurements of a 100 nm transducer deposited using a CHA Modified Mark-40 e-beam evaporator, which was used for all transducer depositions. Transducer thermal conductivity was calculated by measuring the in-plane electrical conductivity of the transducer using the van der Pauw method and applying the Wiedemann-Franz law. An uncertainty of 5% was assigned to transducer conductivity due to the use of the transducer thickness as an input to the van der Pauw method. Volumetric heat capacity was available in peer-reviewed literature for all the samples measured in this work. In most cases, the uncertainty was not reported alongside the literature values and a nominal uncertainty of 5% was used.

The uncertainty of the experimental phase data was calculated by taking five phase measurements at each heating frequency, and using the mean and standard deviation of the data set to define a normal probability distribution function (PDF) for each heating frequency. These PDFs can be used to generate new sets of data and the generated data is fit to the set of generated input parameters to obtain a simulated measurement of thermal conductivity. The process of generating data, generating input parameters, and fitting for thermal conductivity is repeated until the set of best-fit thermal conductivity values converges to a normal distribution (typically after ~2000 trials). An example of the Monte Carlo histogram using this approach for the in-plane thermal conductivity of c-Si is shown in Figure 22.

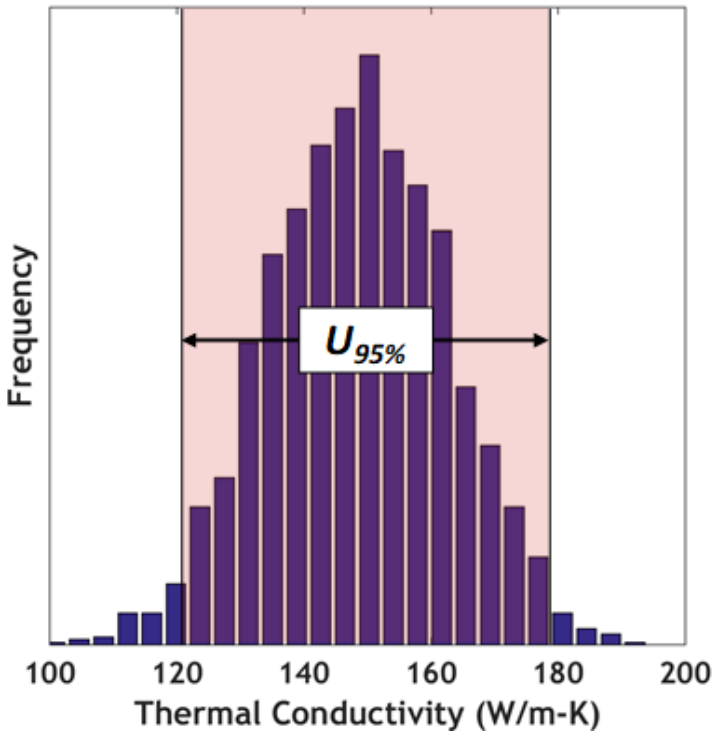

Figure 22 - Uncertainty distribution for thermal conductivity of c-Si based on the parameter values and uncertainties in Table III. 95% of the outcomes fall between 122.8 W/m-K and 179.9 W/m-K, yielding a measured thermal conductivity of 151±28.5 W/m-K.

Once the outcome distribution is obtained, a 95% confidence interval is used to quantify the uncertainty in the fitting parameter. This approach is more conservative than reporting the uncertainty at one standard deviation, albeit at a perceived higher uncertainty.

4.1.7 Direct Measurement of the Thermal Conductivity Accumulation Function

Heating frequency is a useful mechanism for adjusting sensitivity, but it also may have implications for measurement of nanoscale phenomena. One current hypothesis is phonons with mean free path longer than the penetration depth are governed by ballistic transport and therefore have reduced contributions to the observed thermal conductivity.[43, 45] However, reaching such high heating frequencies (> 30 MHz for c-Si) is not a trivial task for two reasons: (1) the magnitude of the FDTR signal, formulated in Equation 32, reduces exponentially as heating frequency increases, (2) the capacitive coupling from the high voltage cables (most notably the cable from the amplifier to the EOM) to the low signal cable leaving the PD increases with frequency, and (3) the magnitude of ambient noise is generally higher in the MHz range because 30-300 MHz is the frequency band used for the vast majority of terrestrial applications (*e.g.*, TV & radio). The result is that the signal-to-noise ratio decreases dramatically as frequency increases, and for most traditional FDTR set-ups the signal magnitude becomes comparable to the noise at around 20 MHz.[37, 45] The trend of signal and noise amplitude versus frequency is plotted in Figure 23. It should be noted that the data presented in Figure 23 was taken directly from the FDTR set-up used for this work and the noise levels may be different for set-ups used elsewhere.

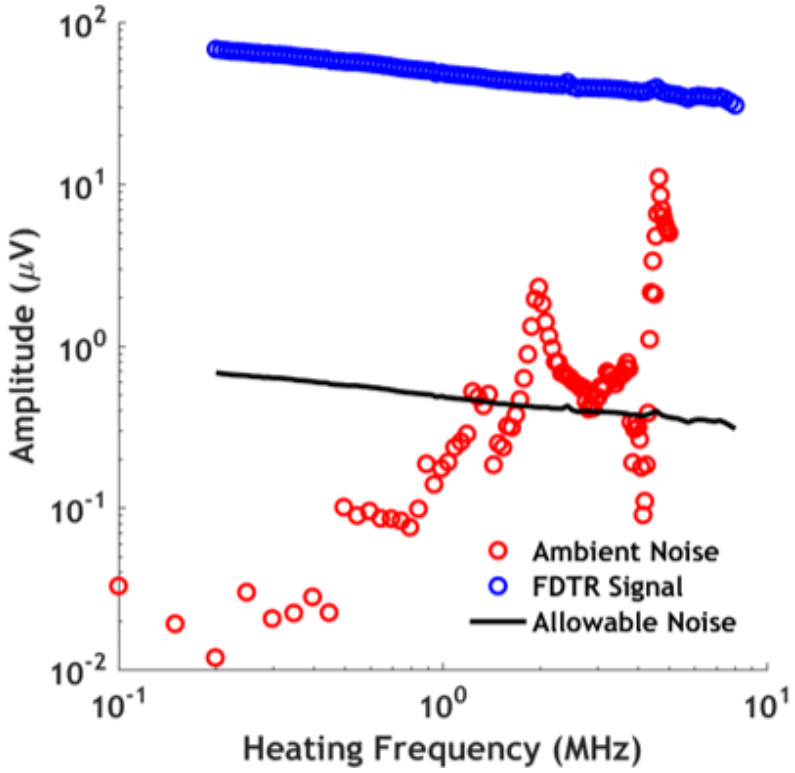

Figure 23 - (a) Magnitude of FDTR signal and ambient noise versus frequency. Ambient noise is negligible at low heating frequencies (f < 1 MHz) but exceeds the threshold for allowable noise around 2 MHz. The threshold for allowable noise is based on a heuristic signal-to-noise ratio of 100. The minimum ambient noise is found at 200 kHz.

Broadband FDTR (BB-FDTR) is an augmentation of traditional FDTR that eliminates coherent noise sources by heterodyning the reflected pump and probe signals. BB-FDTR, described in detail by Regner et al.[45], requires an additional EOM to be placed after the sample. The second EOM is operated at a modulation frequency f_2, where f_2 is the modulation frequency of the first EOM offset by the frequency for which ambient noise is minimized. In the case of Figure 23, where the minimum ambient noise is found at 200 kHz, the second EOM would operate at $f_2=f+200\ kHz$. The reflected pump and probe beams, both modulated at heating frequency f, pass through the second EOM and the exiting beams contain frequency components at the sum and difference of the frequencies

of the two EOMs, f_2+f and f_2-f. It is important make two points: (1) the second EOM preserves the phase difference between the pump and the probe, and (2) the low-frequency component of the mixed signal will always coincide with the point of minimum ambient noise. Therefore, the f_2+f component can be discarded using a low-pass filter and the phase information contained in the low frequency component can be obtained with minimal interference from outside sources.

Efforts to reproduce the frequency-dependent thermal conductivity reported by Regner et al. for c-Si[45] were ultimately unsuccessful. The experimental setup described in this work was used to measure a sample of c-Si. This sample was then taken to Carnegie Melon University and measured in the exact setup reported by Regner et al. The difference between the two measurements exceeded the uncertainty bounds when the penetration depth exceeded 2 μm. A comparison between the two measurements is shown in Figure 24. The difference between the two measurements of the same sample suggests the existence of another (uncontrolled) parameter (potentially spot size) that can affect the frequency-dependent thermal conductivity in either (or both) of the experimental setups.

Experimental measurements by Wilson et al.[47] suggest that the frequency-dependent reduction in thermal conductivity is also related to the anisotropy of the transducer-sample assembly (i.e., heat conducts in-plane through the Au transducer at a different rate than through-plan through the sample), primarily occurring in the through-plane direction while the in-plane thermal conductivity remains unaffected due to the beam spot size being much larger than the phonon mean free paths in c-Si. Therefore, an important step towards improving the reliability of frequency-dependent thermal

conductivity measurements using FDTR is to augment the ability of FDTR to measure anisotropic thermal conductivities accurately.

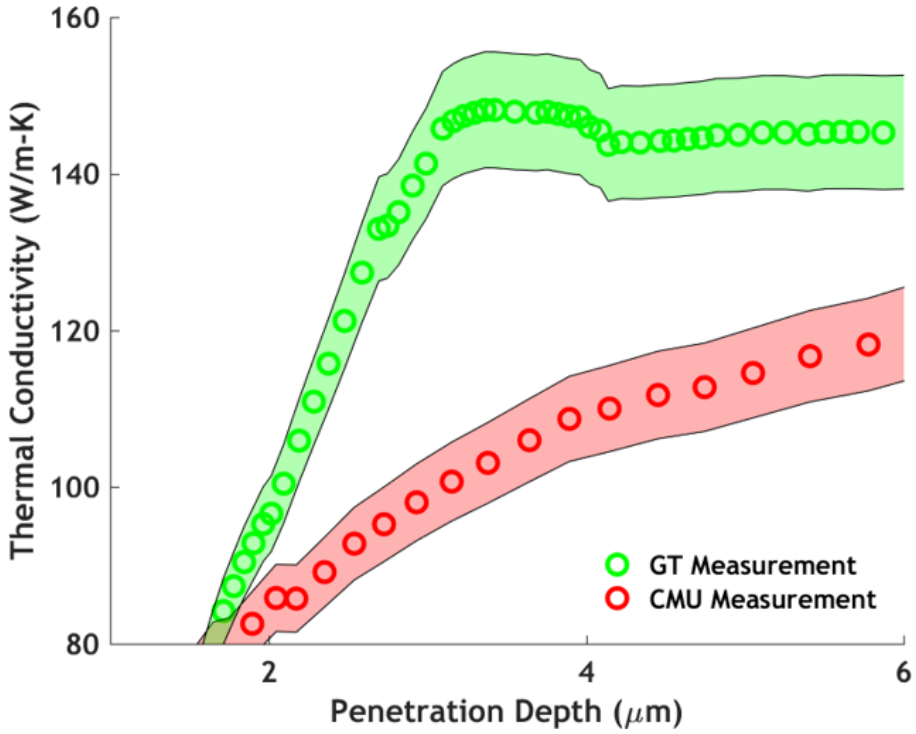

Figure 24 - Thermal conductivity of c-Si as a function of thermal penetration depth. The same sample showed different trends when measured by two different setups, suggesting that the reduction in thermal conductivity may be dependent on the experimental setups.

4.2 Beam-Offset FDTR for Measurement of Anisotropic Samples

High-frequency FDTR measurements may be able to provide insights into the failure of Fourier theory at small length scales.[36, 43, 45] However, Wilson and Cahill suggest that the independent length scales in an FDTR experiment (spot size and penetration depth) can cause an anisotropic reduction in thermal conductivity which can only be interpreted if both the in-plane and through-plane thermal conductivities are measured simultaneously.[47] The ability of FDTR to measure the through-plane thermal

conductivity of thin-films has been robustly demonstrated[38, 39, 121], but in-plane measurements have proven more difficult due to the high thermal conductivity of the metal transducer.[48] Beam offset has been shown to improve the sensitivity of time-domain thermoreflectance (TDTR) to in-plane thermal conductivity and recent advancements in TDTR methodologies by Feser et al. have demonstrated the ability to resolve the full thermal conductivity tensors.[48, 122] In-plane thermal conductivity measurements using FDTR with co-aligned beams have been demonstrated on anisotropic Mo/Si multilayers[123], but the uncertainty of this approach can be prohibitive (>100%) in the case of thin films and small spot sizes.[120] The inability to use a small spot size for these measurements is particularly problematic because in-plane heat spreading is negligible when the spot size is large, resulting in minimal measurement sensitivity to in-plane thermal conductivity.[46] Moving forward, the ability of FDTR to simultaneously measure in-plane and through-plane thermal conductivity with low uncertainty and with a small spot size (~ 3 μm) is a crucial step towards experimental efforts to directly observe phonon transport at the nanoscale.

In this section, we present a peer-reviewed method for the simultaneous measurement of $k_\perp$ and $k_\parallel$ using beam-offset frequency domain thermoreflectance (FDTR) with robust uncertainty estimation. The conventional diffusive heat transfer solution is analyzed to show that offset and heating frequency can independently control the sensitivity to directional thermal conductivity and extract values for $\kappa_\parallel$ and $\kappa_\perp$. Numerical uncertainty analyses demonstrate that sweeping both heating frequency and beam offset results in a reduction of measurement uncertainty. This modified measurement technique

is demonstrated on crystalline alumina (c-Al_2O_3), amorphous alumina (a-Al_2O_3), quartz, fused silica, and highly-oriented pyrolytic graphite (HOPG).

4.2.1 Analytical Solution for Beam-Offset FDTR

The analytical solution for beam-offset FDTR, first demonstrated by Feser et al.[48], builds on the Hankel transform framework from Equation 29. The spatial intensity profile of the offset probe beam is given by

$$p_s(x,y) = \frac{2A_s}{\pi w_1^2} exp(-\frac{2[(x-x_0)^2 + y^2]}{w_1^2}, \tag{37}$$

where A_s is the total power of the probe beam and x_0 is probe offset distance. For the case of isotropic in-plane properties (*i.e.* transport can be described entirely by radial and through-plane thermal conductivities), the intensity profile from Equation 37 can be transformed to the equivalent profile

$$p_s(r) = \frac{1}{2\pi}\int_0^{2\pi} \frac{2A_S}{\pi w_1^2} \exp\left(\frac{-2[(r\cos\theta - x_0)^2 + (r\sin\theta)^2]}{w_1^2}\right) d\theta, \tag{38}$$

which can be integrated directly to obtain

$$p_s(r) = \frac{2A_S}{\pi w_1^2} \exp\left(\frac{-2(r^2 + x_0^2)}{w_1^2}\right) I_0\left(\frac{4x_0 r}{w_1^2}\right). \tag{39}$$

The Hankel transform of the intensity profile in Equation 39 yields

$$P_s(s) = \frac{A_S}{\pi} \exp\left(-\left[\left(\frac{x_0\sqrt{2}}{w_1} \right)^2 + \left(\frac{\pi w_1 s}{\sqrt{2}} \right)^2 \right] \right) \times \sum_{n=0}^{\infty} \frac{1}{(n!)^2} \left(\frac{x_0\sqrt{2}}{w_1} \right)^{2n} \ell_n \left(\frac{w_1 s}{\sqrt{2}} \right), \quad (40)$$

where the polynomial ℓ_n is defined recursively by

$$\ell_{n+1}(x) = -\frac{1}{x}\left[\left(\pi^2 x^3 - x \right) \ell_n(x) + \left(\frac{1}{4\pi^2} - x^2 \right) \frac{d\ell_n}{dx} + \frac{x}{4\pi^2} \frac{d^2\ell_n}{dx^2} \right], \quad (41)$$

where the first term of the polynomial is given by $\ell_0 = \pi$. The multilayer heat transfer solution presented in Section 4.1.4. can be applied to samples with anisotropic thermal conductivity by modifying the term in Equation 32 to

$$u_n = \left[4\pi^2 s^2 \eta + {q_n}^2 \right]^{1/2}, \quad (42)$$

where $\eta = \kappa_\perp / \kappa_\parallel$ is termed the anisotropy ratio.

4.2.2 Sensitivity Analysis for Beam-Offset FDTR

The potential for beam-offset FDTR to measure anisotropic samples can be quantified using a sensitivity analysis (see Section 4.1.5.). To ensure unique results when fitting to multiple parameters simultaneously, the measurement domain should include separate regions of high and low sensitivity. Sensitivity thresholds of $S_\beta > 0.2$ for "high" sensitivity and $S_\beta < 0.05$ for "low" sensitivity are defined relative to the noise fluctuations. If a 5% change in a given parameter will cause a change in the signal that is detectable above ambient noise (see Figure 23) then it is considered to have high sensitivity. If a

parameter can change by 20% before creating a detectable change in the signal, then it is considered to have low sensitivity. The results of an exemplary sensitivity analysis on single-crystal quartz are shown in Figure 25 with the sample parameters listed in Table 4.

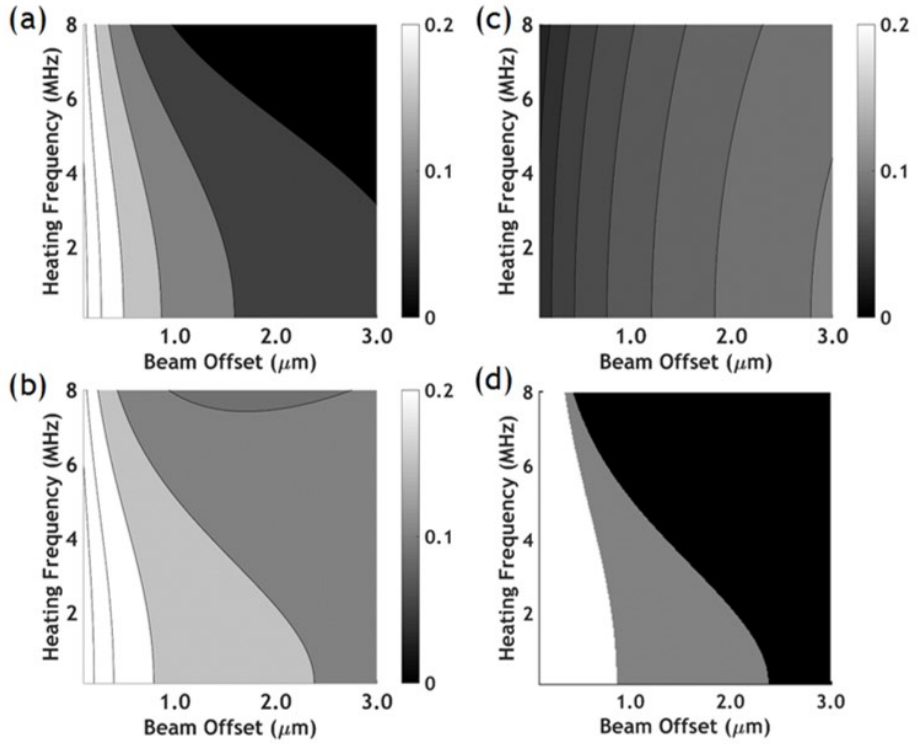

Figure 25 - Sensitivity analysis results for single-crystal quartz with input parameters listed in Table III. (a) Sensitivity to in-plane thermal conductivity as a function of beam offset and heating frequency. Regions of high (white), moderate (gray), and low (black) sensitivity are all found within the domain. (b) Sensitivity to through-plane thermal conductivity. (c) Sensitivity to thermal interface conductance demonstrates low sensitivity to G across the entire domain. (d) Combined sensitivity shows regions where measurement is sensitive to both in-plane and through-plane thermal conductivity (white), only to through-plane conductivity (gray), and insensitivity to both (black).

The sensitivity to the thermal interface conductance between the transducer and sample is low across the entire domain (see Figure 25(c)). Therefore, inaccuracies in the measured value of G are unlikely to propagate into the measurement uncertainty of $\kappa_{\perp}$ and

$\kappa_{\parallel}$. The combined sensitivity plot in Figure 25(d) shows how using both heating frequency and beam offset creates regions in the measurement domain that are sensitive to both $\kappa_{\perp}$ and $\kappa_{\parallel}$ (white), as well as regions that are only sensitive to $\kappa_{\perp}$ (gray). This result for single-crystal quartz cannot be achieved without sweeping through different values of beam offset, thereby demonstrating the expanded capabilities of beam-offset FDTR as compared to traditional FDTR. However, in situ measurements of beam offset are challenging and practical measurements must rely on precise instrumentation to reliably control the beam offset distance.

Table 4 - Nominal parameters for quartz used in the sensitivity analysis shown in Figure 25.

Property	Nominal Value	Uncertainty
$C_{transducer}$	2.5 MJ/m^3-K	5%
$k_{transducer}$	220 W/m-K	5%
$L_{transducer}$	110 nm	3%
w_{probe}	2.0 μm	3%
w_{pump}	3.2 μm	4%
L_{sample}	500 μm	N/A
C_{sample}	1.65 MJ/m^3-K	5%
$\kappa_{\perp}$	6.5 W/m-K	10%
$\kappa_{\parallel}$	9.8 W/m-K	19%
G	51 MW/m^2-K	22%

4.2.3 Offset Instrumentation

To precisely offset the probe beam, a Picomotor mirror mount (Newport Model 8807) with an open-loop driver (Newport Model 8742) is used. The mirror is controlled using high-precision piezo-actuators with each actuator "step" corresponding to a change in angle of 0.7 μrad. The probe beam passes through several optical elements between the

Picomotor mirror and the sample, so it is necessary to calibrate changes in mirror angle to changes in spatial positioning of the probe beam on the sample. These calibrations were performed using a scanning slit beam profiler (DataRay Beam'R2) with a spatial resolution of 100 nm, which allows for the full resolution of the focused laser spots. The calibration results are shown in Figure 26.

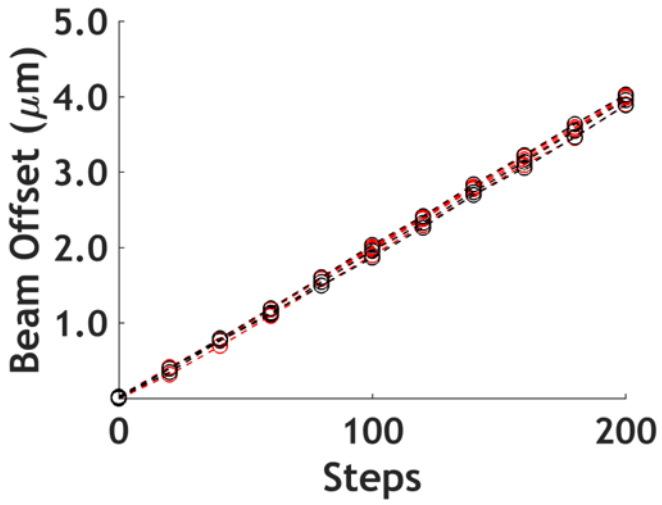

Figure 26 - Picomotor calibration shows consistent linear relationship between actuator steps and offset distance. The five data sets were taken at 1-day intervals and show a day-to-day variation of 4%.

The results from Figure 26 demonstrate that, although the probe's positioning is consistently linear with respect to Picomotor steps, the slope of this relationship would vary each day by as much as 4%. Therefore, we calibrate the Picomotor before and after each measurement to get an accurate estimate of the beam offset distances and to ensure that the calibration does not drift over the course of the measurement.

4.2.4 Measurement Results for Offset-Beam FDTR

Figure 27 compares the measured values of both $\kappa_{\parallel}$ and $\kappa_{\perp}$ to their respective literature values. Overall, the through-plane measurement results show good agreement with nominal literature values across the range of conductivities (~1-25 W/m-K). However, the uncertainty for the in-plane thermal conductivity for low thermal conductivity materials is large, particularly in fused silica, amorphous alumina, and HOPG. The surface roughness of HOPG created uncertainty in the transducer thickness which propagated into the final measurement uncertainty. For amorphous alumina and fused silica, we attribute the high uncertainty to large in-plane heat spreading in the Au transducer; the majority of in-plane heat spreading occurs in the transducer (not the sample), and the penetration depth is much smaller than the spot size due to the low thermal conductivity of the sample. The mismatch in length scales results in very little in-plane heat transfer, which causes the measurement to be less sensitive to the in-plane thermal conductivity of the sample.[48]

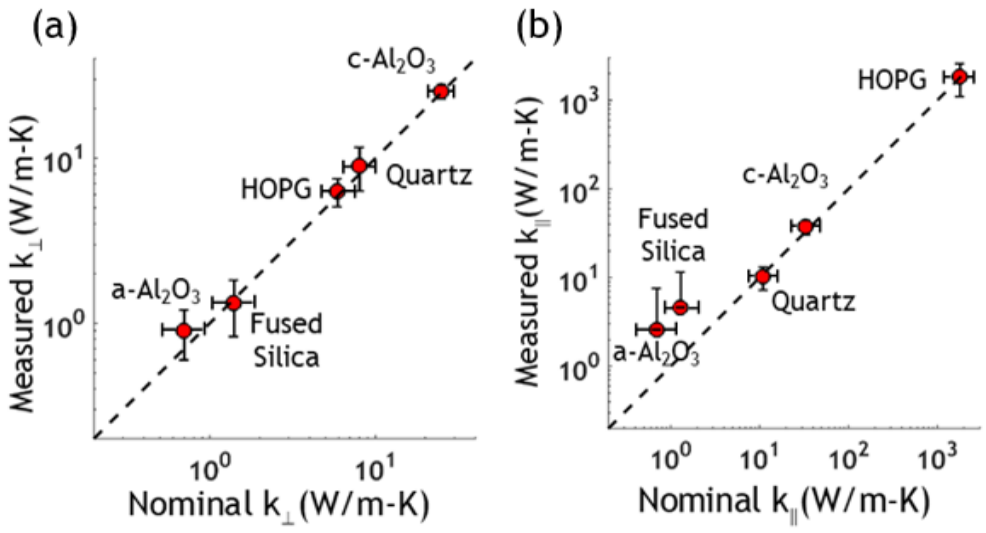

Figure 27 - (a) Comparison between measured and nominal values for $\kappa_{\parallel}$. Vertical error bars indicate measurement uncertainty and horizontal bars indicate uncertainty in nominal value. (b) Comparison between measured and nominal values for $\kappa_{\perp}$. The bottom half of the error bars are omitted for a-Al_2O_3 and fused silica.

4.3 Feasibility of Beam-Offset FDTR for Measurements on np-Si

Using FDTR to measure the phonon MFP contributions in np-Si could provide valuable insight into the mechanisms of thermal conductivity reduction. However, the conclusion from this work is that the current state of offset FDTR would not be capable of making a reliable measurement of np-Si. This conclusion is based on two insights presented in this work: (i) beam-offset FDTR has a limited capability to measure anisotropic samples with low thermal conductivity and (ii) beam-offset FDTR has a limited ability to obtain unique values for $\kappa_{\parallel}$ and $\kappa_{\perp}$ at frequencies beyond 2 MHz. The first conclusion is evident from the high uncertainties for a-Al_2O_3 and fused silica seen in Figure 27(b). Experimental work by Liu et al. suggests the high thermal conductivity of the transducer ($\kappa_{Au} \approx 314$ W/m-K) combined with the low thermal conductivity of the substrate causes most of the heat to spread within the transducer, and results in low measurement sensitivity to the in-plane

thermal conductivity of the sample .[124] Evidence for the second conclusion can be seen in Figure 25(d) where the gray region, which represents the measurement region that is sensitive only to through-plane conductivity, disappears at higher frequencies. Since the values of $\kappa_{\parallel}$ and $\kappa_{\perp}$ should be frequency-dependent, it is critical that the fitting procedure yields unique conductivity values at all frequencies. However, since a high frequency measurement will either be sensitive to both parameters simultaneously or neither parameter, the fitting procedure will be unable to yield unique values for $\kappa_{\parallel}$ and $\kappa_{\perp}$.

CHAPTER 5. CONCLUSION

The replacement of VCT with a low-GWP cooling technology would make an immediate and meaningful reduction in the severity of global warming. TECs represent a promising alternative to VCT but have limited commercial applications due to their high cost, which is in part driven by the high cost of traditional thermoelectric materials such as bismuth telluride. Silicon is a promising alternative to traditional thermoelectric materials due to its natural abundance, low cost, and the wealth of industrial knowledge associated with silicon production and manufacturing. Both n-type and p-type silicon have desirable electrical properties at degenerate doping levels ($n \sim 10^{20}$), but the high lattice thermal conductivity of bulk silicon limits its potential for thermoelectric applications.

The purpose of this work is to investigate the potential for silicon's lattice thermal conductivity to be reduced via nanostructuring and develop fabrication and synthesis methods to produce silicon thermoelectric materials. The first chapter presents peer-reviewed literature, including experimental and theoretical studies, to highlight the difference in the length scales associated with phonon and electron transport, and examines a variety of nanostructuring techniques (e.g. nanowires, porous membranes, np-Si) that have exploited this mismatch to achieve selective reductions in the lattice thermal conductivity of silicon. The first chapter also includes a review of experimental investigations into the MFP accumulation of phonons in silicon, which could be used to validate theoretical studies and inform the fabrication of nanostructured silicon to achieve further reductions in lattice thermal conductivity.

The second chapter reviews the fundamentals of charge transport and phonon transport in semiconductors. Formulations for electrical conductivity and the Seebeck coefficient are presented using the band theory model, and the temperature-dependence of the Fermi level is used to explain the physical origins of the Seebeck coefficient. The relationship between doping concentration and the Fermi level is used to establish an optimum doping concentration for thermoelectric applications, which occurs at around $\sim 10^{20}$ atoms/cm^3 for silicon at room temperature. The transport of phonons in silicon is formulated through an augmentation of the Holland model. The augmented model, which is an original contribution of this work, uses an empirical fitting procedure to predict the size-dependent thermal conductivity of silicon as a function of doping concentration. This contribution is particularly relevant to the study of np-Si due to the large variation in length scales and doping concentrations.

The third chapter includes a description of the np-Si fabrication process and the rationale behind each step, experimental measurements of the effective thermoelectric properties for both n-type and p-type samples, characterization results on the microstructure and atomic composition of the np-Si samples, and a numerical model that incorporates the material characterization results into the augmented Holland model to predict the effective thermoelectric properties for comparison with the experimental measurement results. The numerical model was fit to the experimental measurements of κ_{eff} and σ_{eff} to establish characteristic neck sizes r_κ and r_σ. The values for r_σ were significantly higher than the values for r_κ, suggesting that the experimentally-observed reductions in lattice thermal conductivity were stronger than those predicted by the numerical model. This discrepancy was attributed to shortcomings of the Holland model

at small length scales and assumptions about the spherical nature of the particles in the numerical model. Furthermore, the model underpredicted the contribution of the gaseous pores to κ_{eff}. However, these results are consistent with experimental measurements by Buonanno et al.[110] and analytical modeling by Bahrami et al.[111], who attribute the pressure-dependent thermal conductivity of porous packed-bed materials to interstitial gas pockets that form at the interface between particles.

The fourth chapter focuses on the use of frequency-domain thermoreflectance to develop experimental insights into the size-dependent thermal conductivity of silicon. Efforts to reproduce the frequency-dependent thermal conductivity reported by Regner et al. for c-Si[45] were ultimately unsuccessful, and the disagreement between the measurements could be attributed to the existence of an uncontrolled length scale. Wilson and Cahill suggested that FDTR and TDTR measurements are governed by two relevant length scales, spot size and penetration depth, and these length scales cause independent reductions in the measured thermal conductivity for the in-plane and through-plane directions, respectively.[47] Traditional FDTR measurements lack sensitivity to in-plane thermal conductivity, so an augmentation of frequency-domain thermoreflectance using offset beams was developed to improve in-plane sensitivity. However, the ability of beam-offset FDTR to measure np-Si was limited due to low measurement sensitivity for thermally-insulating materials ($\kappa \sim 1$ W/m-K) and at heating frequencies beyond ~ 2 MHz.

The conclusions and intellectual contributions of this work can be presented by answering three key questions:

To what degree can the thermal conductivity of np-Si be reduced to create a high-performance thermoelectric material?

Experimental measurements of the TE properties of np-Si at room temperature showed a strongly selective reduction in the effective thermal conductivity for both p-type and n-type samples. An effective thermal conductivity of 1.1±0.1 W m^{-1} K^{-1} at standard atmospheric pressure (101 kPa) and 0.67±0.07 W m^{-1} K^{-1} at reduced pressure (~ 1 Pa) was observed for both p-type and n-type samples, whereas the power factor is only reduced by a factor of 2.3x and 8.3x for the p-type and n-type samples, respectively. The effective electrical conductivities of the p-type samples were measured at 25.1±2.6 kS/m and 26.5±2.6 kS/m with Seebeck coefficients of 173±19 μV/K and 178±19 μV/K, respectively. The effective electrical conductivities of the n-type samples were measured at 18.7±1.5 kS/m and 18.9±1.5 kS/m with Seebeck coefficients of -180±20 μV/K and -181±20 μV/K, respectively.

The electronic contribution to thermal conductivity, according to the Wiedemann-Franz law, comprises between 20-25% of the total thermal conductivity in the np-Si samples at reduced pressure, whereas the electronic contribution to thermal conductivity in bulk silicon is ~0.2% at similar doping concentrations. Further reductions in lattice thermal conductivity, on the order of ~15%, were estimated based on the modification to the phononic density-of-states that would occur if the structure were perfectly periodic. However, there is no clear path to achieve a phononic crystal using the fabrication methods from this work.

To what degree is the reduction in thermal conductivity observed in np-Si consistent with current understanding of phonon transport in c-Si?

An augmentation of the Holland model was developed to model the phonon transport in c-Si. The augmented model, which was an original contribution of this work, used an empirical fitting procedure to predict the thermal conductivity of silicon as a function of size and doping concentration. This was particularly important for the study of np-Si due to the large variations in length scales as well as the segregation of dopant atoms observed during APT analysis. The augmented model was incorporated into a numerical model, based on the sintered-sphere geometry described by Ashby, to examine the relationship between the neck size, material composition, and effective thermal conductivity of np-Si. However, the magnitude of the selective reduction in thermal conductivity could not be explained by the numerical model.

The characteristic neck sizes that yield agreement between the numerical model and experimental thermal conductivity measurements are 26 nm and 28 nm for the p-type and n-type samples, respectively. However, the characteristic neck sizes for electrical conductivity are 281 nm and 98 nm for the p-type and n-type samples, respectively. The discrepancy between the characteristic neck sizes for electrical conductivity and thermal conductivity suggest that the selective reduction in thermal conductivity is stronger than predicted by the augmented Holland model developed for this work. Plausible explanations for this discrepancy include: (1) the diminished accuracy of the Holland model at small length scales due to its simplistic view of phonon transport[108], and (2) the introduction of defects during the milling process, which are not accounted for in the numerical model. [27] The application of atomistic simulations to predict the spatially-dependent thermal

conductivity of np-Si could provide insight into whether the discrepancy between the neck sizes is primarily driven by inaccuracies of the Holland model or the simplifying assumptions used in the model geometry.

The numerical model also under predicts the pressure-dependence of the effective thermal conductivity. Experimental measurements indicate that the gaseous pores contribute roughly ~30% of the effective thermal conductivity at ambient pressure, but the numerical model predicts a contribution of only ~13%. However, this discrepancy is consistent with studies on the effective thermal conductivity of porous packed-bed materials, where the strongly pressure-dependent thermal conductivity is attributed to gas pockets that form due to surface roughness at the interface between adjacent particles.[110, 111] This explanation would also be consistent with the suggestion by Bux et al. that defects are formed around the surface of the silicon particles during the milling process. [27]

To what degree can frequency-domain thermoreflectance (FDTR) be used to make observations about thermal transport in np-Si?

The present work failed to reproduce the frequency-dependent thermal conductivity observed by Regner et al.[43], suggesting that an uncontrolled length scale (potentially spot size) may affect the relationship between frequency and measured thermal conductivity. The spot radius for measurements by Regner et al. was 3.2 μm whereas the spot radius in this work was 2 μm. This observation is consistent with observations made by Wilson et al. that the reduction in measured thermal conductivity can be anisotropic, with spot size

controlling the reduction in in-plane thermal conductivity and penetration depth controlling the reduction in through-plane thermal conductivity.[47]

This work presented a novel, peer-reviewed method for making anisotropic thermal conductivity measurements[117], which was successfully applied to measure the anisotropic thermal conductivity of sapphire, highly-oriented pyrolytic graphite, and quartz. However, the technique was unable to measure the in-plane thermal conductivity of thermally-insulating samples ($\kappa \sim 1$ W/m-K) such as amorphous alumina and fused silica. For these samples, the penetration depth (~300 nm) was much smaller than the beam diameter (4 μm). The mismatch in the length scales causes minimal in-plane heat transfer, and therefore minimal sensitivity to the in-plane thermal conductivity of the sample. This is particularly true for higher measurement frequencies which would result in a further reduction of the penetration depth. Based on its inability to resolve the in-plane thermal conductivity of insulating materials, particularly at high frequencies, it was ultimately concluded that this method has a limited ability to study the MFP contributions of np-Si using high-frequency measurements.

REFERENCES

1. Chua, K.J., S.K. Chou, and W.M. Yang, *Advances in heat pump systems: A review.* Applied Energy, 2010. **87**(12): p. 3611-3624.
2. Xu, Y., et al., *The role of HFCs in mitigating 21st century climate change.* Atmos. Chem. Phys., 2013. **13**(12): p. 7.
3. Montzka, S., et al., *Scientific assessment of ozone depletion: 2010.* Global Ozone Research and Monitoring Project-Report No. 51, 2011.
4. Patil, P.J. and P.A.M. Patil, *Review on Thermoelectric Devices.* Int. J. Emerg. Technol. Adv. Eng., 2013. **3**(10): p. 681-688.
5. Bell, L.E., *Cooling, Heating, Generating Power, and Recovering Waste Heat with Thermoelectric Systems.* Science, 2008. **321**(5895): p. 1457-1461.
6. Rowe, D.M., et al. *Effect of a limit to the figure-of-merit on thermoelectric generation*. in *Collection of Technical Papers. 35th Intersociety Energy Conversion Engineering Conference and Exhibit (IECEC) (Cat. No.00CH37022)*. 2000.
7. Vineis, C.J., et al., *Nanostructured Thermoelectrics: Big Efficiency Gains from Small Features.* Advanced Materials, 2010. **22**(36): p. 3970-3980.
8. Schierning, G., et al., *Silicon-based nanocomposites for thermoelectric application.* physica status solidi (a), 2016. **213**(3): p. 497-514.
9. Yuji, O., et al., *Thermoelectric properties of heavily boron- and phosphorus-doped silicon.* Japanese Journal of Applied Physics, 2015. **54**(7): p. 071301.
10. Xie, W., et al., *High thermoelectric performance BiSbTe alloy with unique low-dimensional structure.* Journal of Applied Physics, 2009. **105**(11): p. 113713.
11. Tang, J., et al., *Holey Silicon as an Efficient Thermoelectric Material.* Nano Letters, 2010. **10**(10): p. 4279-4283.
12. Hopkins, P.E., et al., *Origin of reduction in phonon thermal conductivity of microporous solids.* Applied Physics Letters, 2009. **95**(16): p. 161902.
13. Fang, J. and L. Pilon, *Scaling laws for thermal conductivity of crystalline nanoporous silicon based on molecular dynamics simulations.* Journal of Applied Physics, 2011. **110**(6): p. 064305.
14. Cahill, D.G., et al., *Nanoscale thermal transport.* Journal of Applied Physics, 2003. **93**(2): p. 793-818.
15. Boor, J.d., et al., *Temperature and structure size dependence of the thermal conductivity of porous silicon.* EPL (Europhysics Letters), 2011. **96**(1): p. 16001.
16. Benedetto, G., L. Boarino, and R. Spagnolo, *Evaluation of thermal conductivity of porous silicon layers by a photoacoustic method.* Applied Physics A, 1997. **64**(2): p. 155-159.
17. Hopkins, P.E., et al., *Thermal Conductivity in Nanoporous Gold Films during Electron-Phonon Nonequilibrium.* Journal of Nanomaterials, 2008. **2008**: p. 7.
18. Song, D. and G. Chen, *Thermal conductivity of periodic microporous silicon films.* Applied Physics Letters, 2004. **84**(5): p. 687-689.

19. Regner, K.T., et al., *Broadband phonon mean free path contributions to thermal conductivity measured using frequency domain thermoreflectance.* Nature communications, 2013. **4**: p. 1640.
20. Shiomi, J., *Research Update: Phonon engineering of nanocrystalline silicon thermoelectrics.* APL Materials, 2016. **4**(10): p. 104504.
21. Valalaki, K., P. Benech, and A. Galiouna Nassiopoulou, *High Seebeck Coefficient of Porous Silicon: Study of the Porosity Dependence.* Nanoscale Research Letters, 2016. **11**(1): p. 201.
22. Hicks, L. and M.S. Dresselhaus, *Thermoelectric figure of merit of a one-dimensional conductor.* Physical review B, 1993. **47**(24): p. 16631.
23. Schierning, G., *Silicon nanostructures for thermoelectric devices: a review of the current state of the art.* physica status solidi (a), 2014. **211**(6): p. 1235-1249.
24. Boukai, A.I., et al., *Silicon nanowires as efficient thermoelectric materials*, in *Materials For Sustainable Energy: A Collection of Peer-Reviewed Research and Review Articles from Nature Publishing Group*. 2011, World Scientific. p. 116-119.
25. Yadav, A., K. Pipe, and M. Shtein, *Fiber-based flexible thermoelectric power generator.* Journal of Power Sources, 2008. **175**(2): p. 909-913.
26. Sztein, A., et al., *GaN-based integrated lateral thermoelectric device for micro-power generation.* Applied physics express, 2009. **2**(11): p. 111003.
27. Bux, S.K., et al., *Nanostructured bulk silicon as an effective thermoelectric material.* Advanced Functional Materials, 2009. **19**(15): p. 2445-2452.
28. Minnich, A., et al., *Bulk nanostructured thermoelectric materials: current research and future prospects.* Energy & Environmental Science, 2009. **2**(5): p. 466-479.
29. Chen, G., *Recent trends in thermoelectric materials research III.* Semiconductors and Semimetals, 2001. **71**(1): p. 203-259.
30. Jeng, M.-S., et al., *Modeling the thermal conductivity and phonon transport in nanoparticle composites using Monte Carlo simulation.* Journal of Heat Transfer, 2008. **130**(4): p. 042410.
31. Kessler, V., et al., *Thermoelectric Properties of Nanocrystalline Silicon from a Scaled‐Up Synthesis Plant.* Advanced engineering materials, 2013. **15**(5): p. 379-385.
32. Henry, A.S. and G. Chen, *Spectral phonon transport properties of silicon based on molecular dynamics simulations and lattice dynamics.* Journal of Computational and Theoretical Nanoscience, 2008. **5**(2): p. 141-152.
33. Qiu, B., et al., *First-principles simulation of electron mean-free-path spectra and thermoelectric properties in silicon.* EPL (Europhysics Letters), 2015. **109**(5): p. 57006.
34. Esfarjani, K., G. Chen, and H.T. Stokes, *Heat transport in silicon from first-principles calculations.* Physical Review B, 2011. **84**(8): p. 085204.
35. Chen, G., *Nanoscale energy transport and conversion: a parallel treatment of electrons, molecules, phonons, and photons*. 2005: Oxford University Press.
36. Regner, K.T., J.P. Freedman, and J.A. Malen, *Advances in Studying Phonon Mean Free Path Dependent Contributions to Thermal Conductivity.* Nanoscale and Microscale Thermophysical Engineering, 2015. **19**(3): p. 183-205.

37. Schmidt, A.J., R. Cheaito, and M. Chiesa, *A frequency-domain thermoreflectance method for the characterization of thermal properties.* Review of Scientific Instruments, 2009. **80**(9): p. 094901.
38. Liu, J., et al., *Simultaneous measurement of thermal conductivity and heat capacity of bulk and thin film materials using frequency-dependent transient thermoreflectance method.* Review of Scientific Instruments, 2013. **84**(3): p. 034902.
39. Malen, J.A., et al., *Optical Measurement of Thermal Conductivity Using Fiber Aligned Frequency Domain Thermoreflectance.* Journal of Heat Transfer, 2011. **133**(8): p. 081601-081601.
40. Schmidt, A.J., X. Chen, and G. Chen, *Pulse accumulation, radial heat conduction, and anisotropic thermal conductivity in pump-probe transient thermoreflectance.* Review of Scientific Instruments, 2008. **79**(11): p. 114902.
41. Minnich, A.J., et al., *Thermal conductivity spectroscopy technique to measure phonon mean free paths.* Physical review letters, 2011. **107**(9): p. 095901.
42. Koh, Y.K. and D.G. Cahill, *Frequency dependence of the thermal conductivity of semiconductor alloys.* Physical Review B, 2007. **76**(7): p. 075207.
43. Regner, K.T., et al., *Broadband phonon mean free path contributions to thermal conductivity measured using frequency domain thermoreflectance.* Nature Communications, 2013. **4**: p. 1640.
44. Freedman, J.P., et al., *Universal phonon mean free path spectra in crystalline semiconductors at high temperature.* Scientific reports, 2013. **3**: p. 2963.
45. Regner, K.T., S. Majumdar, and J.A. Malen, *Instrumentation of broadband frequency domain thermoreflectance for measuring thermal conductivity accumulation functions.* Review of Scientific Instruments, 2013. **84**(6): p. 064901.
46. Minnich, A.J., et al., *Thermal Conductivity Spectroscopy Technique to Measure Phonon Mean Free Paths.* Physical Review Letters, 2011. **107**(9): p. 095901.
47. Wilson, R.B. and D.G. Cahill, *Anisotropic failure of Fourier theory in time-domain thermoreflectance experiments.* Nature Communications, 2014. **5**: p. 5075.
48. Feser, J.P. and D.G. Cahill, *Probing anisotropic heat transport using time-domain thermoreflectance with offset laser spots.* Review of Scientific Instruments, 2012. **83**(10): p. 104901.
49. Maznev, A.A., J.A. Johnson, and K.A. Nelson, *Onset of nondiffusive phonon transport in transient thermal grating decay.* Physical Review B, 2011. **84**(19): p. 195206.
50. Hua, C. and A.J. Minnich, *Transport regimes in quasiballistic heat conduction.* Physical Review B, 2014. **89**(9): p. 094302.
51. Regner, K., A.J. McGaughey, and J.A. Malen, *Analytical interpretation of nondiffusive phonon transport in thermoreflectance thermal conductivity measurements.* Physical Review B, 2014. **90**(6): p. 064302.
52. Minnich, A.J., et al., *Quasiballistic heat transfer studied using the frequency-dependent Boltzmann transport equation.* Physical Review B, 2011. **84**(23): p. 235207.
53. Vermeersch, B., et al., *Superdiffusive heat conduction in semiconductor alloys. I. Theoretical foundations.* Physical Review B, 2015. **91**(8): p. 085202.

54. Vermeersch, B., et al., *Superdiffusive heat conduction in semiconductor alloys. II. Truncated Lévy formalism for experimental analysis.* Physical Review B, 2015. **91**(8): p. 085203.
55. Ohishi, Y., et al., *Thermoelectric properties of heavily boron-and phosphorus-doped silicon.* Japanese Journal of Applied Physics, 2015. **54**(7): p. 071301.
56. Poudel, B., et al., *High-thermoelectric performance of nanostructured bismuth antimony telluride bulk alloys.* Science, 2008. **320**(5876): p. 634-638.
57. Garg, J., et al., *Role of disorder and anharmonicity in the thermal conductivity of silicon-germanium alloys: A first-principles study.* Physical review letters, 2011. **106**(4): p. 045901.
58. Ju, Y. and K. Goodson, *Phonon scattering in silicon films with thickness of order 100 nm.* Applied Physics Letters, 1999. **74**(20): p. 3005-3007.
59. Ward, A. and D. Broido, *Intrinsic phonon relaxation times from first-principles studies of the thermal conductivities of Si and Ge.* Physical Review B, 2010. **81**(8): p. 085205.
60. Callaway, J., *Model for Lattice Thermal Conductivity at Low Temperatures.* Physical Review, 1959. **113**(4): p. 1046-1051.
61. Holland, M.G., *Analysis of Lattice Thermal Conductivity.* Physical Review, 1963. **132**(6): p. 2461-2471.
62. Glassbrenner, C. and G.A. Slack, *Thermal conductivity of silicon and germanium from 3 K to the melting point.* Physical Review, 1964. **134**(4A): p. A1058.
63. Chung, J.D., A.J.H. McGaughey, and M. Kaviany, *Role of Phonon Dispersion in Lattice Thermal Conductivity Modeling.* Journal of Heat Transfer, 2004. **126**(3): p. 376-380.
64. Norris, R.H., G.E.C.C. Research, and D. Center, *Fluid Flow Data Book*. 1970: Genium Publishing Corporation.
65. R. H. Olsson, I. and I. El-Kady, *Microfabricated phononic crystal devices and applications.* Measurement Science and Technology, 2009. **20**(1): p. 012002.
66. Kushwaha, M.S., et al., *Theory of acoustic band structure of periodic elastic composites.* Physical Review B, 1994. **49**(4): p. 2313-2322.
67. Hopkins, P.E., et al., *Reduction in the Thermal Conductivity of Single Crystalline Silicon by Phononic Crystal Patterning.* Nano Letters, 2011. **11**(1): p. 107-112.
68. Nava, R., et al., *Akhiezer damping and the thermal conductivity of pure and impure dielectrics.* Physical Review B, 1976. **14**(2): p. 800-807.
69. Daly, B.C., et al., *Picosecond ultrasonic measurements of attenuation of longitudinal acoustic phonons in silicon.* Physical Review B, 2009. **80**(17): p. 174112.
70. Barrett, H.H. and M.G. Holland, *Critique of Current Theories of Akhieser Damping in Solids.* Physical Review B, 1970. **1**(6): p. 2538-2544.
71. Jiang, P., L. Lindsay, and Y.K. Koh, *Role of low-energy phonons with mean-free-paths >0.8 μm in heat conduction in silicon.* Journal of Applied Physics, 2016. **119**(24): p. 245705.
72. Lifshitz, R. and M.L. Roukes, *Thermoelastic damping in micro-and nanomechanical systems.* Physical review B, 2000. **61**(8): p. 5600.
73. Cuffe, J., et al., *Lifetimes of confined acoustic phonons in ultrathin silicon membranes.* Physical review letters, 2013. **110**(9): p. 095503.

74. Kunal, K. and N. Aluru, *Akhiezer damping in nanostructures.* Physical Review B, 2011. **84**(24): p. 245450.
75. Holt, A.C. and M. Ross, *Calculations of the Gr\"uneisen Parameter for Some Models of the Solid.* Physical Review B, 1970. **1**(6): p. 2700-2705.
76. Maris, H.J., *Physical Acoustics*. Academic, ed. W.P.M.a.R.N. Thurston. Vol. 8. 1971, New York.
77. Maznev, A.A., *Onset of size effect in lattice thermal conductivity of thin films.* Journal of Applied Physics, 2013. **113**(11): p. 113511.
78. Pomerantz, M., *Temperature Dependence of Microwave Phonon Attenuation.* Physical Review, 1965. **139**(2A): p. A501-A506.
79. Yang, N., et al., *Thermal interface conductance between aluminum and silicon by molecular dynamics simulations.* Journal of Computational and Theoretical Nanoscience, 2015. **12**(2): p. 168-174.
80. Liao, B., et al., *Significant reduction of lattice thermal conductivity by the electron-phonon interaction in silicon with high carrier concentrations: A first-principles study.* Physical review letters, 2015. **114**(11): p. 115901.
81. Broido, D.A., et al., *Intrinsic lattice thermal conductivity of semiconductors from first principles.* Applied Physics Letters, 2007. **91**(23): p. 231922.
82. Baroni, S., et al., *Phonons and related crystal properties from density-functional perturbation theory.* Reviews of Modern Physics, 2001. **73**(2): p. 515-562.
83. Green, M.S., *Markoff Random Processes and the Statistical Mechanics of Time‐Dependent Phenomena. II. Irreversible Processes in Fluids.* The Journal of Chemical Physics, 1954. **22**(3): p. 398-413.
84. Kubo, R., *Statistical-Mechanical Theory of Irreversible Processes. I. General Theory and Simple Applications to Magnetic and Conduction Problems.* Journal of the Physical Society of Japan, 1957. **12**(6): p. 570-586.
85. Indris, S., D. Bork, and P. Heitjans, *Nanocrystalline oxide ceramics prepared by high-energy ball milling.* Journal of Materials Synthesis and Processing, 2000. **8**(3-4): p. 245-250.
86. Koch, C. and Y. Cho, *Nanocrystals by high energy ball milling.* Nanostructured Materials, 1992. **1**(3): p. 207-212.
87. de Boer, G.B., et al., *Laser diffraction spectrometry: Fraunhofer diffraction versus Mie scattering.* Particle & Particle Systems Characterization, 1987. **4**(1‐4): p. 14-19.
88. Mudroch, A., *Manual of physico-chemical analysis of aquatic sediments*. 2017: Routledge.
89. Naito, M., et al., *Effect of particle shape on the particle size distribution measured with commercial equipment.* Powder Technology, 1998. **100**(1): p. 52-60.
90. Pincus, A. and L. Shipley, *The role of organic binders in ceramic processing.* Ceram. Ind, 1969. **92**(106-109): p. 146.
91. Jones, S.W., *Diffusion in silicon.* IC Knowledge LLC, 2008: p. 1-68.
92. Ashby, M.F., *A first report on sintering diagrams.* Acta Metallurgica, 1974. **22**(3): p. 275-289.
93. Lebrun, J.-M., *Investigation of Oxidation and Sintering mechanisms of Silicon powders for photovoltaïc applications*. 2012, Institut National Polytechnique de Grenoble - INPG.

94. Frenkel, J., *Viscous flow of crystalline bodies under the action of surface tension.* J. phys., 1945. **9**: p. 385.
95. Bo, Q., et al., *First-principles simulation of electron mean-free-path spectra and thermoelectric properties in silicon.* EPL (Europhysics Letters), 2015. **109**(5): p. 57006.
96. Kuczynski, G.C., *Self-diffusion in sintering of metallic particles.* JOM, 1949. **1**(2): p. 169-178.
97. ASTM, in *B193-16 Standard Test Method for Resistivity of Electrical Conductor Materials*. 2016, ASTM International: West Conshohocken, PA.
98. ASTM, in *E977-05(2014) Standard Practice for Thermoelectric Sorting of Electrically Conductive Materials*. 2014, ASTM International: West Conshohocken, PA.
99. Bentley, R.E., *Handbook of Temperature Measurement Vol. 3: The Theory and Practice of Thermoelectric Thermometry*. Vol. 3. 1998: Springer Science & Business Media.
100. Gustafsson, S.E., *Transient plane source techniques for thermal conductivity and thermal diffusivity measurements of solid materials.* Review of scientific instruments, 1991. **62**(3): p. 797-804.
101. Wray, K.L. and T.J. Connolly, *Thermal conductivity of clear fused silica at high temperatures.* Journal of Applied Physics, 1959. **30**(11): p. 1702-1705.
102. Kasai, T., K. Horio, and A. Kobayashi, *Improvement of conventional polishing conditions for obtaining super smooth surfaces of glass and metal works.* CIRP Annals-Manufacturing Technology, 1990. **39**(1): p. 321-324.
103. Buonaquisti, A.D., W. Carter, and P.H. Holloway, *Diffusion characteristics of boron and phosphorus in polycrystalline silicon.* Thin Solid Films, 1983. **100**(3): p. 235-248.
104. Swaminathan, B., et al., *Diffusion of arsenic in polycrystalline silicon.* Applied Physics Letters, 1982. **40**(9): p. 795-798.
105. Dowling, N.E., *Mechanical behavior of materials: engineering methods for deformation, fracture, and fatigue*. 2012: Pearson.
106. G. K. Batchelor, F.R.S., R. W. O'Brien, *Thermal or electrical conduction through a granular material.* Proceedings of the Royal Society of London. A. Mathematical and Physical Sciences, 1977. **355**(1682): p. 313.
107. Van Antwerpen, W., C. Du Toit, and P. Rousseau, *A review of correlations to model the packing structure and effective thermal conductivity in packed beds of mono-sized spherical particles.* Nuclear Engineering and design, 2010. **240**(7): p. 1803-1818.
108. McGaughey, A.J.H. and M. Kaviany, *Quantitative validation of the Boltzmann transport equation phonon thermal conductivity model under the single-mode relaxation time approximation.* Physical Review B, 2004. **69**(9): p. 094303.
109. Jain, A. and A.J.H. McGaughey, *Effect of exchange–correlation on first-principles-driven lattice thermal conductivity predictions of crystalline silicon.* Computational Materials Science, 2015. **110**: p. 115-120.
110. Buonanno, G., et al., *Experimental and theoretical modeling of the effective thermal conductivity of rough steel spheroid packed beds.* Journal of heat transfer, 2003. **125**(4): p. 693-702.

111. Bahrami, M., M.M. Yovanovich, and J.R. Culham, *Effective thermal conductivity of rough spherical packed beds.* International Journal of Heat and Mass Transfer, 2006. **49**(19-20): p. 3691-3701.
112. Cahill, D.G., *Analysis of heat flow in layered structures for time-domain thermoreflectance.* Review of Scientific Instruments, 2004. **75**(12): p. 5119-5122.
113. P.E. Raad, P.L.K., M.G. Burzo, *Thermo-Reflectance Thermography For Submicron Temperature Measurements.* Electronics Cooling, 2008. **14**.
114. Favaloro, T., J.-H. Bahk, and A. Shakouri, *Characterization of the temperature dependence of the thermoreflectance coefficient for conductive thin films.* Review of Scientific Instruments, 2015. **86**(2): p. 024903.
115. Carslaw, H.S. and J.C. Jaeger, *Conduction of heat in solids*. 2d ed. ed. 1959, Oxford :: Clarendon Press.
116. Feldman, A., *Algorithm for solutions of the thermal diffusion equation in a stratified medium with a modulated heating source.* High Temperatures. High Pressures, 1999. **31**(3): p. 293-298.
117. Rodin, D. and S.K. Yee, *Simultaneous measurement of in-plane and through-plane thermal conductivity using beam-offset frequency domain thermoreflectance.* Review of Scientific Instruments, 2017. **88**(1): p. 014902.
118. Bougher, T.L., et al., *Thermal Boundary Resistance in GaN Films Measured by Time Domain Thermoreflectance with Robust Monte Carlo Uncertainty Estimation.* Nanoscale and Microscale Thermophysical Engineering, 2016: p. 1-11.
119. Papadopoulos, C.E. and H. Yeung, *Uncertainty estimation and Monte Carlo simulation method.* Flow Measurement and Instrumentation, 2001. **12**(4): p. 291-298.
120. Yang, J., E. Ziade, and A.J. Schmidt, *Uncertainty analysis of thermoreflectance measurements.* Review of Scientific Instruments, 2016. **87**(1): p. 014901.
121. Dames, C. and G. Chen, *1ω,2ω, and 3ω methods for measurements of thermal properties.* Review of Scientific Instruments, 2005. **76**(12): p. 124902.
122. Feser, J.P., J. Liu, and D.G. Cahill, *Pump-probe measurements of the thermal conductivity tensor for materials lacking in-plane symmetry.* Review of Scientific Instruments, 2014. **85**(10): p. 104903.
123. Medvedev, V.V., et al., *Anisotropy of heat conduction in Mo/Si multilayers.* Journal of Applied Physics, 2015. **118**(8): p. 085101.
124. Liu, J., G.-M. Choi, and D.G. Cahill, *Measurement of the anisotropic thermal conductivity of molybdenum disulfide by the time-resolved magneto-optic Kerr effect.* Journal of Applied Physics, 2014. **116**(23): p. 233107.